TECHNICAL MEMORANDUM

196

Computation of optimal perturbations using a local projection operator: a winter case study

R. Buizza

Research Department

October 1993

This paper has not been published and should be regarded as an Internal Report from ECMWF.
Permission to quote from it should be obtained from the ECMWF.

European Centre for Medium-Range Weather Forecasts
Europäisches Zentrum für mittelfristige Wettervorhersage
Centre européen pour les prévisions météorologiques à moyen

ABSTRACT

Ensemble prediction is an attempt to estimate the probability distribution of forecast states, through a finite sample of non-linear deterministic integrations of a numerical weather prediction model. At the European Centre for Medium-Range Weather Forecasts (ECMWF), it is based on 32+1 (control) model integrations at horizontal triangular truncation T63, with 19 vertical levels. The initial conditions of the perturbed forecasts are generated from optimal perturbations, which identify the directions in the phase space of the system which guarantee the maximum growth of the total energy of the perturbation over a fixed time interval. Since ECMWF is mainly interested in predicting the atmospheric flow over the northern hemisphere, in particular over the European region, optimal perturbations are chosen to give different forecasts in this region. One of the problems we faced during the first months of ensemble prediction was that, on some occasions, the spread between the perturbed and the control forecasts appeared to be small. The case study analyzed in this paper, the 14.02.93, represents an extreme among these cases. On that period, for three consecutive days, the two unperturbed forecasts (the control T63L19, and the high resolution operational forecast), and all the perturbed forecasts of the ensemble system were very similar over the European region. A second problem, closely related to this one, that we had to prevent, was the inability of the system to identify optimal perturbations which amplify over the northern hemisphere during the warm seasons, when the relative instability of the northern hemisphere is smaller than the instability of the southern hemisphere. Both these problems can be cured by introducing a constraint when computing the optimal perturbations, i.e. by localizing the region over which the growth has to be maximized. To introduce this constraint, the Local Projector Operator is defined and applied in the computation of the optimal perturbations. We prove that its application prevents the second problem completely. Moreover, we show how the action of this operator can increase the spread among the ensemble members.

1. INTRODUCTION

On the 19th of December 1992, at the European Centre for Medium-Range Weather Forecasts (ECMWF), the new Ensemble Prediction System (hereafter EPS) started (*Molteni and Palmer*, 1993; *Mureau et al*, 1993). It is based on the execution of an ensemble of non-linear deterministic integrations of a numerical weather prediction model (*Epstein*, 1969, and *Leith*, 1974). The EPS is run three days a week, from each saturday, sunday and monday 12GMT analysis. Each member of the ensemble system is a 10-day time integration of a version of the ECMWF model at horizontal truncation T63, with 19 vertical levels. So, every week, for each of these days, 34 10-day forecasts are generated: the high resolution ECMWF operational forecast, run at horizontal truncation T213 with 31 vertical levels, the unperturbed (control) and 32 perturbed T63L19 members of the EPS.

Optimal perturbations, i.e. structures that grow fastest over a finite time interval, can be used to construct the initial conditions (IC) of the members of the ensemble. In particular, at ECMWF, the 32 IC of the perturbed forecasts are generated adding to the unperturbed IC a linear combination of 16 optimal perturbations, automatically selected among the most unstable ones.

The importance of optimal transient instabilities was first suggested by *Lorenz* (1965). Subsequently, *Farrell* (1982) investigated their structures in simple models, and concluded that they are likely to identify the directions in the phase space of the systems that are more active dynamically (*Farrell*, 1988). Calculations of these finite time interval instabilities have been performed by *Borges and Hartmann* (1992) using a barotropic model, and by *Molteni and Palmer* (1993) using T21 barotropic and T21, 3-level quasi-geostrophic (QG) models.

The optimal perturbations can be computed, in the linear approximation, applying the adjoint technique, which uses the tangent forward and adjoint versions of the full non-linear model. The adjoint technique has been proposed by *Lorenz* (1965), and subsequently applied to variational data assimilation studies (*Lacarra and Talagrand*, 1988; *Courtier et al*, 1991). Note that, since the fastest growing perturbations are the singular vectors (SVs) of the propagator of the forward tangent model with the largest singular values (*Buizza et al*, 1993), hereafter we will use the abbreviation SVs to identify them.

Since the systems studied by *Borges and Hartmann* (1992), and by *Molteni and Palmer* (1993) were not too large, they could identify the optimal perturbations using a conventional matrix algorithm. Instead of this, their identification needs sophisticated algorithms when the analyzed system is a primitive equation (PE) model with a large number of degrees of freedom. *Buizza* (1992), and *Buizza et al* (1993) described how a Lanczos algorithm (*Strang*, 1986) can be applied to compute optimal perturbations using a T21, 19-

level adiabatic PE system. In their studies, they applied the adjoint technique defining the norm of a perturbation as its total energy.

As regards SV sensitivity to model parametrizations, *Buizza et al* (1993) studied the impact of a non-linear normal mode (NNMI) procedure on the optimal perturbations, and they concluded that, during the SV computation, it should be restricted to not more than the 5 gravest modes. Comparing the effectiveness of the PE versus the QG perturbations, they found that, when added to an analysis field to define the IC for a perturbed forecast, the PE optimal perturbations were able to give a larger deviation from the unperturbed trajectory than the QG 3-level optimal structures. They also concluded that a planetary boundary layer parametrization is essential to eliminate "non-meteorological" low-level perturbations which arise in the adiabatic computation, but do not correspond to unstable modes of the real atmosphere. On a later paper, *Buizza* (1993) studied this problem, and showed that the implementation of a simple vertical diffusion and surface drag scheme can solve this problem.

Another very important aspect to be taken into account when using optimal perturbations for ensemble predictions, is the definition of the optimisation time interval (hereafter OTI), i.e. the time over which the growth is maximized. *Buizza* (1993) concluded that time intervals shorter than 12 hours should be avoided, and suggested that the choice of time intervals longer than 36 hours could give unstable perturbations with characteristic time long enough to give large divergence among the trajectories also after the non-linear effects become important, i.e. after 2-3 days.

These studies defined the ECMWF configuration used to compute the SVs, which is also used for the experiments described in this paper:

- total energy norm;
- NNMI applied to the 5 gravest modes;
- adiabatic model + vertical diffusion and surface drag parametrization;
- 36 hours OTI, except when clearly pointed out.

At ECMWF, the computation of the optimal perturbations uses a new model, the Integrated Forecasting System (IFS), developed by ECMWF and Météo-France for, inter alia, the application of 4-D variational data assimilation (*Courtier et al*, 1991; *Rabier and Courtier*, 1992). We refer to *Buizza* (1992) for details on the computation of the SVs using a Lanczos algorithm.

Since ECMWF is mainly interested in predicting the atmospheric flow over the northern hemisphere (NH), and in particular over the European region, we would like the EPS to be able to give an estimate of the probability distribution of forecast states for this region. In particular, we would like the EPS to be able

to estimate the tails of the probability distribution function. This can be achieved if the spread among the EPS members is large enough. A small spread among the EPS trajectories can indicate that the situation is very easily predictable, and so that we can expect a very skilful unperturbed forecast. On the contrary, it can indicate that the perturbations are too small, or are located in regions that do not influence the prediction over Europe. We want to investigate if we can have a better EPS performance changing the computation of the optimal perturbations, i.e. by introducing a constraint to the physical space where the perturbations can maximize their growth. This can be achieved using a projection operator, the Local Projection Operator (LPO), which acts on the state vector in the physical space.

In fact, the analysis of the EPS performance during the 1991-1992 winter season indicates that, on some occasions, the spread among the EPS members seemed to be too small (statistics on the EPS performance during the winter 1992-1993 and spring 1993 seasons will be presented in a subsequent paper). The first part of this work will deal with this problem. We will focus on a case study, the 14.02.93, which represents an extreme among the small-spread cases. Considering each of the three ensembles run during the week-end of the 14.02.93, all the perturbed forecasts up to forecast (fc) day 7 seemed to be small "variationi sul tema" of the unperturbed forecast.

The second part of this work will study a problem very closely related to the one highlighted above. As already mentioned, we are interested in having a large spread among the EPS trajectories in the NH. This means that, when selecting 16 among the 30-35 perturbations that the IFS system provides to generate the perturbed IC, we discard the ones growing in the southern hemisphere (SH). When the relative instability of the NH is smaller than the instability of the SH, the first 30-35 SVs identified by the IFS system appear to be characterized by maximum growth over the SH. This makes impossible to run the EPS, since all the computed SVs are rejected by the selection algorithm. We will show how this problem starts being present in April-May, and becomes very important during summer. We will see how the use of the LPO can avoid this problem completely.

Section 2 below describes the atmospheric situation of the 14.02.93 and the following days. In section 3 we introduce the LPO. In section 4 we study the impact of the LPO on the SVs definition and on the forecast spread for the 14.02.93 case. In this section we also give some details on the automatic algorithm that selects the 16 optimal perturbations to be used to construct the perturbed IC. Section 5 shows the impact of the LPO when computing the SVs for spring and summer cases. Some conclusions are drawn in section 6.

2. THE 14.02.93 CASE

Fig 1 shows the 500 hPa geopotential height analysis for the 14th and the 21st of February, corresponding to fc day 7 of the integrations started on the 14th. On the 14th, a region of high pressure dominates the European area, with a south-westerly flow north of the British Isles and a trough over Russia; a zonal flow characterizes the circulation over the Asian continent and western Pacific, with a deep ridge north-west of the Rockies and a region of low pressure over eastern Canada. During the following days the flow over Europe becomes more zonal. At fc day 2 the ridge north-west of the Rockies evolves into a blocking structure, which lasts till fc day 7, when a strong north, north-westerly flow characterizes the flow over the British Isles. The trough over central Europe deepens during the following days, and a cut-off low develops at fc day 9 over the Adriatic sea.

To evaluate the skill of the 14.02.93 forecasts, we computed the anomaly correlation (AC) between the unperturbed and perturbed forecasts and the analysis, for different areas and fc days. In particular, we focus on the forecast skill at fc day 7 over the European region defined by the following coordinates: latitude between 30N and 75N degrees, and longitude between 20W and 45E degrees. Fig 2a shows the spread between each perturbed forecasts and the control, while Fig 2b shows the skill of the perturbed and unperturbed forecasts. The high resolution T213L31 model forecast is very skilful up to fc day 5, with AC values higher than 80%, decreasing to 65% at fc day 6, increasing the day after to 71% and then gently decreasing to 52% at fc day 10. The control forecast is slightly worse than the high resolution model, especially between fc day 7 and 9 when AC values of 44% are reached. The perturbed forecasts start diverging from the control at fc day 2, all of them characterized by worse scores during the following 3 days. If we consider Fig 2a, we can see that, at fc day 5, the spread between the perturbed forecasts and the control reaches a local maximum, and that, at fc day 4 and 5, some of the perturbed forecasts have AC scores less than 70%. Then, around fc day 7, the perturbed trajectories get closer to the control, while later on they start diverging again, with approximately half of them better and half of them worse than the control.

Fig 3 shows the 500 hPa geopotential height forecasts over Europe, predicted by the two unperturbed and by the EPS members run with starting date the 12GMT of the 14.02.93 and verifying date the 21.02.93 (t+168h). The first two panels of the first row show the control and the high resolution forecasts and the third panel shows the verifying analysis for the European region. The stamps on the successive rows refer to the perturbed members. The first impression is that all the forecasts are very similar, all characterized by a trough over northern Europe, with a north-eastern tilt, and a north-westerly wind over the British islands. A closer inspection reveals that there are some but very small differences between them. A close look at the scores of the single forecasts of Fig 2, reveals that the two EPS members number 29 and 31 have a very high AC score at fc day 7, 79%. At fc day 7, if compared to the unperturbed forecasts, 2 of the EPS

members have AC score equal and 6 better than the T213 L31 forecast, and 1 of the EPS members have AC score equal and 17 better than the control (see Table 1).

Concluding, the analysis of the spread between the perturbed and the control forecasts, shown in Fig 2, confirms that the trajectories of the EPS forecasts in the phase space of the system are very close at fc day 7, with none of them able to develop a flow closer to the analysis (see Fig 3).

If we consider the EPS forecasts of the integrations started on the 13th and on the 15th and verifying at the same date, the same picture can be drawn. Very low spread between the forecasts, with only three of the more recent forecasts started on the 15th giving a trough with a more correct tilt over Europe. Generally speaking, the scores of the 14.02.93 forecasts were better than the scores of the 13.02.93 and the scores of the 15.02.93 better than the scores of the 14.02.93.

The fact that, for the same verification date, 99 different forecasts with different IC and starting dates gave very similar predictions suggests that the situation over Europe of the weekend of the 14.02.93 was very stable and very predictable. This was really the case, and both the control and the T213 forecasts were characterized by AC scores higher than average. Nevertheless, we would have liked at least few of the EPS forecasts to diverge more from the control and possibly to have higher AC scores for as long as fc day 10.

The low spread between the EPS forecasts at fc day 7, and the fact that very skilful forecasts with AC over 80% up to fc day 10 are missing, can be related to the following reasons:

- the directions in the phase space of the system identified by the perturbations chosen to generate the perturbed initial conditions were not amplifying over Europe at fc day 7;

- the directions identified were amplifying over Europe, but their initial amplitudes were too small to generate enough spread;

- adding small although optimal perturbations to the unperturbed initial conditions can not compensate for model errors.

The perturbation amplitudes are defined after comparing them with an estimate of the analysis error field (see section 4), and we think that increasing the amplitude will lead to too large perturbations compared to the estimates. We will investigate this point in another paper, which will study in details the similarities and differences between the perturbations and the error estimates, and which will investigate the possibility of achieving a better agreement between the two fields. So, we will not deal with the second point in this

paper. The first point will be investigated in section 4, while we will comment on the third point in the conclusions.

3. THE LOCAL PROJECTION OPERATOR

The SVs are the direction in the phase space of the system which maximize the norm of a perturbation after a time interval t, called the optimisation time interval:

$$\|x(t)\|^2 = \langle x(t); E\, x(t) \rangle \tag{1}$$

where the matrix E is a matrix of weight factors that in our case defines the total energy norm, and where the vector x represents a perturbation which satisfies the linearized model equations:

$$\frac{dx}{dt} = A_l\, x \tag{2}$$

where $A_l = \frac{\delta A}{\delta x}|_{x(t)}$ is the tangent operator that corresponds to the non-linear model operator $A(x)$. If we indicate the resolvent of equation (2) by $L(t_0;t)$, the norm at time t can be computed as:

$$\|x(t)\|^2 = \langle L\, x_0; E\, L\, x_0 \rangle \tag{3}$$

where x_0 is the IC. Let us suppose that the state vector of the system is defined in the spectral space, as it is the case for the IFS system. We can define the Local Projection Operator T as:

$$T = S^{-1}\, G\, S \tag{4}$$

where S, S^{-1} represent the spectral to grid point and the inverse transformations, and where G represents the multiplication of the state vector in grid point space by a weighting function defined to be 1 inside a localized area, and zero outside. If we apply the operator T to an input state vector, then we have as the output a vector that, in grid point space, is equal to the input one inside the defined local area and is zero outside.

Applying the operator T after the resolvent operator, we can confine the perturbation over the local area defined by the weighting function G:

$$\|x(t)\|^2 = \langle T\, L\, x_0; E\, T\, L\, x_0 \rangle \tag{5}$$

Applying the adjoint technique, the norm of the state vector can be computed as:

$$\|x(t)\|^2 = \langle x_0;\ L^{*E}\, T^{*E}\, E\, T\, L\, x_0 \rangle \tag{6}$$

where L^{*E}, T^{*E} are the adjoint of the operators L, T with respect to the norm defined by the energy weight factor E.

The optimal perturbations constrained to grow over a localized area are the eigenvectors of the operator:

$$L^{*E}\, T^{*E}\, E\, T\, L \qquad (7)$$

with the largest eigenvalues. They are the singular vectors (SVs) of the operator $T\,L$, and they are computed applying a Lanczos algorithm to the operator (7).

4. OPTIMAL PERTURBATIONS GENERATED APPLYING THE LPO

The 32 perturbations added to the control IC to generate the perturbed IC are constructed using 16 selected SVs. The selection of 16 among the 30-35 orthogonal SVs computed by the IFS system is based on the following criteria:

- the SVs with maximum amplitude in the southern hemisphere are neglected;

- the SVs are selected so that to minimize a cost function that compares the SVs with the analysis error;

- a test is made so that the selected SVs do not overlap over the same area.

Since the 16 selected SVs are very localized in space, a phase-space rotation is applied to generate 16 less localized fields. These 16 perturbations are also rescaled in order to have local maxima comparable to the local analysis error. The coefficients of this phase-space rotation are computed applying a minimisation procedure to the ratio between the perturbation amplitude and an estimate of the initial analysis error given by the Optimal Interpolation procedure.

Table 2 reports the characteristics of the 5 IFS configurations used to compute the SVs during our experiments. OPE identifies the characteristics of the operational system. The rational for the c02 and the c03 experiments is to check if the confinement of the SV areas of growth can give a larger spread among the ensemble members. The c04 experiment has been run to identify the SVs that guarantee the maximum growth over the European area. All these experiments have been run with a 36h OTI, a time interval during which the time evolution of small perturbations can be approximated by the linear equation (2). Although we know that the linear approximation can be applied for time intervals not longer than 2-3 days, we decided to run the c05 experiment with the LPO applied to the European area, but with a 7 day OTI. The c05 SVs will give us an indication of the structures and of the areas where the perturbations should have been located to generate the maximum growth over Europe after 7 days.

Before analysing the SVs characteristics, let us remind the reader of the definition of the "similarity index" (*Buizza et al*, 1993) that can be used to compare unstable sub-spaces generated by the SVs of two different

experiments. We define the ***N-dim*** unstable sub-space relative to an experiment as the sub-space of the phase space of the system defined by the first N most unstable perturbations. We can compare the unstable sub-spaces generated by the first N SVs v_i of two experiments A and B using a projection matrix $M(A,B;N)$, defined using the scalar product definition (1), as:

$$m_{i,j}(A,B) = \left(\langle v_i(A);E\, v_j(B)\rangle\right)^2 \tag{8}$$

Each element of this matrix is the squared scalar product between the i -th SV of the A experiment, and the j -th SV of the B experiment. In other words, it represents the amount of the energy of the i -th SV of the A experiment that is explained by the j -th SV of the B experiment. The sum of the matrix elements with a fixed first index represents how well the i -th SV of the A experiment can be reconstructed from a linear combination of the first N SVs of the B experiment.

We define the similarity index of two experiments A,B, which measures the similarity of the unstable sub-spaces generated by the first N SVs of each experiment, as:

$$s\,(A,B;N) = \frac{1}{N}\sum_{i,j=1}^{N} m_{i,j}\,(A,B) \tag{9}$$

Some reference values for the similarity index are listed below:

a) parallel sub-spaces have $s\,(A,B,N) = 100\%$;

b) orthogonal sub-spaces have $s\,(A,B,N) = 0\%$;

c) statistics analysis performed using the first 3 months of EPS results showed that the similarity index between the unstable sub-spaces generated by the first 20 36h-OTI SVs, computed for two consecutive days, has a mean value of $s\,(day;day+1,20) = 50\%$;

d) statistics analysis performed as in point c), but for unstable sub-spaces computed 2 days apart, showed that the similarity index has a mean value of $s\,(day;day+2,20) = 30\%$.

More reference values are reported in *Buizza* (1993).

An indication of the regions where the selected perturbations of one experiments have maximum amplitude, is given by the "overlap factor" field. The overlap factor field gives, for each experiment, the number of selected SVs that cover a specified area, with the area covered by each SV defined to be the area where the local total energy of the SV is larger than 1% of its maximum value.

In sub-section 4.1 we analyze the structure of the OPE SVs. In sub-section 4.2 we analyze the c05 SVs (see Table 2), i.e. the optimal perturbations with maximum growth over Europe after an OTI of 7 days, and we

compare the unstable sub-space generated by these with the OPE SVs. In sub-section 4.3 we analyze the c02, c03 and c04 SVs, optimal perturbations constrained to grow over the NH, over the region of the NH with latitude $\lambda \geq 30$, and over the European region only, during a 36h time period. In sub-section 4.4 we describe the result of an ensemble run using the c03 perturbations.

4.1 The 14.02.93 operation optimal perturbations

Fig 4a shows the overlap factor field at model level 11, and Fig 4b shows the root mean square (RMS) amplitude of the perturbations for the temperature component at model level 11. We can identify three regions of maximum concentration of the SVs in the NH, one located over Sahara and the Arabic peninsula, one over western Pacific and one over the sub-tropical eastern Pacific. Another local maximum is present over central USA. Note that some SVs have structures also in the southern hemisphere (SH), and that very few perturbations are located in the Atlantic storm track. Looking in details at the position of some of the SVs, the 1st and the 3rd SVs are located over western Pacific and eastern Asia, the 2nd, 4th, 5th, 6th, 7th, 12th and 14th SVs over Sahara and the Arabic peninsula, the 8th and the 11th SVs over the sub-tropical eastern Pacific. The 13th SV has two maxima, one over the eastern tropical Pacific and one over north-eastern America, and the 15th SV is located over north-eastern America.

Let us consider the SVs number 1, 2 and 8, each of which is located in one of the three areas of maximum overlap. Panels a), b) and c) of Fig 5 shows their streamfunction at model level 11. We run 6 non-linear T63 L19 integrations, adding and subtracting these very localized and unrotated perturbations to the control IC (after having been rescaled correctly), to study if they have any impact on the flows over Europe at fc day 7. Fig 6 shows the difference between the perturbed and the control 500 hPa geopotential height fields, at fc day 1 (left panels) and 7 (right panels). Note that the contour interval for the right panels is 5 times larger. Figs. 6a and 6b refers to the forecasts run with the IC constructed adding the 1st perturbation, Figs 6c and 6d to the forecasts run with the IC constructed subtracting the 1st perturbation, and so on. It can be clearly seen that after 1 day of non-linear integration, the non-linear effects are still small, although some differences start to appear between the perturbed forecasts generated by adding or subtracting the same unstable structure to the control IC. Fig 6 shows that at fc day 7 only the perturbations localized in the eastern Pacific have an impact on the flow over Europe.

It is worth mentioning that we linearly integrated the SVs for 7 days and we found that the differences between the linear and the non-linear integrations were small up to fc day 2, but quite large after fc day 4. If we consider the 2nd SV, for example, if linearly integrated it is growing over the European area after fc day 3, while its non-linear evolution is not characterized by any amplification over this region (see Fig 6, panels e-h).

We decided to run four more experiments adding and subtracting the unrotated SVs number 13 and 15 (see Figs 5d and 5e). These two SVs were chosen among the others because, when linearly integrated for 7 days, they were giving a very large growth over the European region. The rational for these time integrations is to check, once more, the accuracy and the usefulness of the 7-days linear integrations. Figs 7 and 8 show respectively the 500Pa geopotential height field at fc day 1 and 7 of the integrations with IC generated from these two SVs. It can be clearly seen that these two perturbations have an impact on the flow over Europe. In section 2 we have seen that the EPS members number 29 and 31 were the two forecasts with the highest scores at fc day 7. Their initial conditions were generated adding rotated perturbations defined as linear combinations of the unrotated perturbations. Looking at the matrix that characterizes the linear rotation (not shown) it can be seen that they have, respectively, the largest projection onto the unrotated SVs number 13 and 15. It must be mentioned that the forecasts started with the unrotated initial conditions are characterized by a very large spread, with AC between them and the control of 60% at fc day 2, but that their skills are very low.

4.2 7-day European optimal perturbations

Although the comparison between the linear and the non-linear time integrations of the SVs reported in sub-section 4.1 proved that the two evolutions can be very different when time intervals longer than 2-3 days are considered, we decided to compute the 7-days SVs to try to identify "source regions" where the SVs should have been located to have an impact on the target region considered, i.e. Europe in our case.

Fig 9 shows the first 6 c05 SVs (streamfunction at model level 11) at initial (left panel) and after 7 days of linear integration (right panel). Generally speaking, at initial time they are more spread out in the physical space than the SVs computed with a shorter time interval. The 1st SV has maximum amplitude over the Atlantic, a region where the OPE SVs have almost zero amplitude (see Fig 4). The 2nd SV is essentially located over eastern Pacific and the Sahara, regions were the OPE SVs were also located. The 5th and the 6th SV have maximum amplitude over north-eastern USA, a region of low concentration of OPE SVs. The structure of the fields at the end of the 7 days OTI clearly shows the impact of the LPO in constraining the area of growth of the perturbations (the contour interval at the final time is 20 times larger). Note that the 5th and the 6th SV does not show, at model level 11, the same amplitude as the other four SVs because their amplification factors are 3 times smaller than the amplification factors of the first four SVs. Moreover, note that all the SVs have structures outside the LPO area because the LPO was applied only during their computation by the Lanczos algorithm, but not during their linear time integration.

These and the results reported in sub-section 4.1, indicate that the identification of the Sahara region as one of the "source regions" for SVs with maximum growth over Europe after 7 days is not correct. On the

contrary, the importance of the USA area as a "source region" is supported by the non-linear evolution of the 15th SV (see Figs 7 and 8).

We can compare the OPE with the c05 unstable sub-spaces generated by the first 20 most unstable SVs, using the projection matrix. Table 3 reports the similarity indices computed between different pairs of experiments. The similarity index $s(OPE,c05,20) = 11\%$ indicates that there is a small but not negligible degree of similarity between the two unstable sub-spaces, although they have been computed in very different configurations. The first 4 selected OPE SVs that have the largest projection on the c05 unstable sub-space can be identified using the projection matrix $M(OPE,c05,20)$, and are listed in table 4. Table 4 confirms that the 13th and the 15th OPE SVs have the most similar structures to the c05 SVs. The projection matrix $M(OPE,c05,20)$ identifies also the 2nd and the 8th OPE SVs as SVs with a lower but not negligible similarity. The difference between the linear and the non-linear time evolution shows how dangerous can be to draw conclusions from studies based on the linear approximation only, when this latter is applied for time intervals during which it does not hold. Nevertheless, and being conscious of this limit, the comparison of the c05 SVs with the SVs computed in the other configurations gives useful indications. For example, the comparison of the OPE and c05 unstable sub-spaces confirms that the SVs located in the eastern Pacific, USA and western Atlantic regions are the one that can have the largest impact on the forecast spread over Europe at fc day 7.

4.3 36h localized optimal perturbations

Fig 10 shows the overlap factors of the 16 perturbations selected by the EPS system from the SVs computed in configurations c02 (panel a) and c03 (panel b). If we compare the c02 with the OPE overlap factors, we can see that the restriction of the area of growth to the NH has cancelled the perturbations from the SH, while conserving almost the same pattern in the NH. The high value of the similarity index $s(OPE,c02,20) = 82\%$ indicates that the two unstable sub-spaces are very similar. The impact of restricting the LPO area to points with latitude $\lambda \geq 30N$ have instead a large impact over the eastern sub-tropical Pacific and over the Sahara regions, since these regions of maximum OPE SVs concentration extend south of 30N degrees. Moreover, the c03 overlap factor field shows a maximum value in the north-eastern USA and Atlantic region that was not present in the OPE or the c02 cases.

The analysis of the projection matrix between the OPE and the c02 experiment confirms the similarity between the two unstable sub-spaces (see Table 5). Nevertheless this high similarity, the overlap factor fields are different because of the action of the selection algorithm. The first 12 SVs of both the unstable sub-spaces can be considered identifying the same sub-space, since each of them has at least 70% of its norm explained by its projection on the SVs of the other experiment. These first 12 SVs have been selected

by the selection algorithm for both the c02 and the OPE SVs. The 16th OPE SV was also selected, but this has a very small projection onto the c02 unstable sub-space. On the contrary, the algorithm selected from the c02 SVs the 17th, the 18th and the 20th SV, which have very small projection onto the OPE unstable sub-space. So, the combined action of the LPO during the SV computation, and of the selection algorithm can have an impact on the definition of the initial perturbations.

Table 3 shows that $s(OPE,c03,20) < s(OPE,c02,20)$, and this confirms the comments we made comparing Fig 4a and Fig 10. The fact that $s(OPE,c03,20) \approx s(c02,c03,20)$ indicates that the restriction of the LPO area to the grid points with $\lambda \geq 30N$ has a larger impact than the restriction to the NH only, as it is expected considering the location of the OPE SVs.

We can compare the c02 and the c05 unstable sub-spaces. Although the similarity index has a small value, we can identify the c02 SVs characterized by the largest projection onto the c05 unstable sub-space (table 4 reports the 4 SVs with the largest projection). It is interesting to analyze the area that they cover: the 15th, the 18th and the 20th SVs have maximum amplitude over eastern Pacific and USA, and the 8th SV is localized in the eastern Pacific region. As a cross verification test, table 5 shows that the 8th, 15th and 18th c02 SVs have maximum projection, respectively, onto the 8th, the 13th and the 15th OPE SVs. Instead of this, the 20th c02 SV has maximum projection onto the 19th OPE SV that was not chosen by the selection algorithm.

We conclude this section comparing the OPE, the c02 and the c03 unstable sub-spaces with the sub-space generated from the SVs computed with the LPO applied to the European area (experiment c04). This comparison identifies which of the three sub-spaces can generate the largest spread over Europe after 36h, a time interval for which the linear approximation is valid. Table 3 shows that, among the three, the c03 unstable sub-space is the more similar to the c04 sub-space. The projection matrix $M(c03,c04,20)$ indicates that the first 4 most unstable c04 SVs project more than 50% of their norm onto the unstable sub-space generated by the 16 selected c03 SVs. The same 4 SVs project only 20% of their norm onto the unstable sub-space generated by the selected OPE or c02 SVs.

Since our problem is to try to enlarge the spread among the EPS members over the European region, the results reported above suggest to generate the perturbed IC using the c03 SVs. Sub-section 4.4 describes the results we obtained.

4.4 Skill of an ensemble generated from localized SVs

Fig 11 shows that the spread between the perturbed forecasts and the control, when the perturbed IC are generated from the c03 SVs, is larger than the spread between the OPE perturbed forecasts and the control.

If we consider, for example, the spread at fc day 5, some of the perturbed c03 trajectories have AC smaller than 70% while all the OPE perturbed forecasts have AC greater than 80%. As it was the case for the OPE EPS, the c03 trajectories get closer to the control around fc day 6-7, and then starts diverging with a spread larger than the OPE case.

Comparing Fig 11 and Fig 2 we can see that enlarging the spread induces less skilful perturbed forecasts during the first 4-5 days, but it also increases the chances to have better forecasts at the end of the forecast interval. Some statistics on the c03 scores are reported in Table 1. Table 1 confirms that the EPS forecasts generated from the c03 SVs have a better chance to have higher scores between fc day 7 and 10, but this causes less forecasts to have $60\% < AC < 70\%$. Looking at the skill scores of the single forecasts, two EPS members have very high scores at fc day 7, the 23rd member has 81% AC score and the 26th member has 80% AC score, while for the OPE case the two more skilful members have AC score of 79%.

The analysis of the AC values computed for different areas (e.g. the NH) confirms the general impression that the confinement of the area of possible growth of the perturbations to the points in the physical space with latitude $\lambda \geq 30$, can give a higher probability of having very good forecasts at the end of the forecast interval, but it can also decrease the skill of the perturbed forecasts during the first 4-5 days of integration.

Let us analyze in detail the EPS member number 30 which, between fc day 7 and 10, has the best AC scores among the forecasts generated using the c03 perturbations. Fig 12 shows the 500 hPa geopotential height field at fc day 7. Apart from the trough over Europe that is still represented with a slightly wrong tilt, the general circulation over the western Atlantic and the European sector is well captured. The IC of the 30th member are generated mainly from the 17th c03 SV, as it can be identified looking at the elements of the rotation matrix (not shown). The comparison between the c03 and the c05 unstable sub-spaces identifies this SV as one of the three c03 SVs with the largest projection onto the c05 unstable sub-space (31%, while the c03 SV with the maximum projection is the 6th with 37%). Moreover, the comparison of the c03 and the c04 unstable sub-spaces identifies the 17th and the 13th c03 SVs as the only two among the c03 SVs with a projection greater than 30%, respectively with a total projection value of 67% and 69%. Fig 13 shows the 17th c03 SV at initial time, and after 36h linear integration. Initially, it has maximum amplitude over northern Atlantic and north-western Europe, and it evolves strongly over central and north-eastern Europe. It is worth mentioning that it is almost orthogonal to the OPE unstable sub-space, with only 2 % of its total energy norm explained by the OPE unstable sub-space.

These results indicate that the application of the LPO when computing the SVs permits to generate perturbations which are more efficient in diverging from the control trajectory. This seems to give a better estimate of the tails of the probability distribution of forecast states.

5. IMPACT OF THE LPO ON THE SPRINGTIME SVs

Fig 14 shows the RMS amplitude of the perturbations (temperature at model level 11) that would have been added to the control IC by the operational EPS, for three starting dates, 2, 9 and 16 May 1992. The changing of the season from winter to spring and summer is characterized by a variation in the relative instability of the two hemisphere. During (NH) winter, the most unstable areas are almost completely localized in the NH and so the perturbations added to the control IC generates perturbed trajectory with different flow pattern in the NH. On the contrary, during spring, SVs start being localized in SH. As the season progresses, it gets more and more difficult for the automatic algorithm to select 16 among the 30-35 SVs that the Lanczos algorithm computes, which are not localized in the SH. The comparison of Fig 4b with Fig 14 clearly confirms that this is the case. Two more experiments were run with starting dates 23 and 25 May, 1992: for these two dates the selection algorithm was unable to select the 16 necessary SVs to generate the EPS IC.

Fig 15 shows the RMS amplitude of the perturbations generated from SVs computed with the LPO applied to the physical space with latitude $\lambda \geq 30$. These results show that the impact of the LPO is very large during the spring season. Moreover, experiments run with starting dates 23 and 30 May demonstrated that the inclusion of the LPO is a necessary condition to be able to run the EPS system during the this period of the year.

Table 6 reports the similarity indices computed between the unstable sub-space generated in the two configurations, for the three spring dates. Taking into account also the similarity index between the 14.02.93 OPE and c03 unstable sub-space, we can clearly see that the seasonal variation of the position of the most unstable regions increases the impact of the LPO on the definition of the unstable sub-space.

6. CONCLUSIONS

The analysis of the performance of the new Ensemble Prediction System run at the European Centre for Medium-Range Weather Forecasts during winter 1992-93, indicated that, on some occasions, the spread between the perturbed and the control forecasts were too small to give an accurate estimate of the probability distribution of forecast states. A small spread can indicate that the atmospheric flow is not characterized by instabilities that can be responsible for a very fast amplification of the initial errors that reduces the skill of the forecasts, or it may be related to a poor efficiency of the added perturbations in giving trajectory divergence in the phase space of the system. Model error common to all ensemble members is a further possibility.

A new operator, the Local Projection Operator, has been introduced in the IFS, the new ECMWF model used to compute the optimal perturbations, to constrain the area of possible growth of the perturbations to

localized regions. In the first part of this paper, it has been applied to a case study to see if its action can improve the EPS performances, increasing the spread among the perturbed trajectories.

The analyzed case study, based on forecasts with starting date the 12GMT of the 14.02.93, is an extreme case of very small spread. This is partly due to the very predictable atmospheric flow that characterized the week-end of the 14.02.93, as it has been confirmed by the quite accurate predictions made by the unperturbed forecasts. A second reason that can explain the small spread among the EPS members can be that the optimal perturbations used to construct the IC of the perturbed forecasts were not effective enough.

To test if this was the case, we computed optimal perturbations in four different configurations, and we showed that only few of the selected OPE SVs used to construct the perturbed IC were not located in the "source regions", i.e. regions where the perturbations should be located to have the largest impact over the target area, which is the European region in our case, after 7 days. The "source regions" were identified using the linear approximations for time intervals longer that 2-3 days, that is known to be the limit of validity for the linear approximation. Our results seems to indicate that, if the linear investigations are supported by non-linear studies, they can give very useful indications, in agreement with the non-linear results.

We demonstrated that the action of the LPO to confine the area of possible growth to the physical space with latitude $\lambda \geq 30$, can guarantee a larger spread between the EPS members and the control. Considering the 14.02.93 case study, we proved that this confinement of the area of possible growth of the perturbations can give a better estimate of the tails of the probability distribution of forecast states.

One reason why the spread among the perturbed trajectories increased only slightly, or let us say less than expected, can be related to model errors, as it was mentioned in section 2. Adding small perturbations, although optimal, can not compensate for deficiencies in the model parametrizations. This has been confirmed by the EPS performances during winter '92-'93: when situations difficult to be predicted occur, the control AC score curve drowns with all the perturbed AC score curves, without any of them surviving above the 60% AC line, after fc day 5. Underestimation of analysis error (e.g. poor quality control decisions) could be another reason. Moreover, the use of a simple model in the trajectory computation and the absence of physics (e.g. moist processes) when computing the optimal perturbations can explain the less than expected spread.

Although this first part of our paper presented results of two parallel EPS run, one with localized and one with non-localized SVs, for one date only, other comparisons were made during the implementation of the

EPS at ECMWF for less skilful cases. The results of these cases confirmed the positive impact of the LPO in giving higher chances of having very good forecasts around the end of the forecast interval.

In section 5 we focused on another problem, which is related to the different relative instability of the two hemisphere during the hot or cold seasons. Since ECMWF is mainly interested in estimating the probability distribution of forecast states in the northern hemisphere, the IC of the EPS members have to be constructed from the SVs which guarantee the largest possible spread in this hemisphere. Springtime case studies showed that the LPO is necessary to let the IFS identify optimal perturbations which amplify over the northern hemisphere, when the relative instability of this hemisphere decreases. We showed that this problem starts occurring in spring, and can be fatal during the NH hottest months, and proved that the action of the LPO can cure this problem completely.

The LPO has been introduced in the EPS system on the 19.03.93. The major result of its implementation was the possibility to identify 16 optimal perturbations to generate the initial conditions of the EPS perturbed members during the hot seasons.

ACKNOWLEDGEMENT

We would like to thank F Molteni, T Palmer and A Simmons for the very useful discussion we had during the development of this work.

REFERENCES

Borges, M D and D L Hartmann, 1992. Barotropic instability and optimal perturbations of observed non-zonal flows. J Atmos Sci, 49, 335-354.

Buizza, R, 1992. Unstable perturbations computed using the adjoint technique. ECMWF Tech Memo No. 189, Shinfield Park, Reading RG2 9AX, UK.

Buizza, R, J Tribbia, F Molteni and T N Palmer, 1993. Computation of optimal unstable structures for a numerical weather prediction model. On print by Tellus.

Buizza, R, 1993. Sensitivity of optimal unstable structures. Submitted to Q J R Meteorol Soc.

Courtier, P, C Freydier, J-F Geleyn, F Rabier and M Rochas, 1991. The Arpege project at Météo-France. Proceedings of ECMWF Seminar on "Numerical methods in atmospheric models", Shinfield Park, Reading RG2 9AX, UK, 9-13 September 1991, Vol. 2, 193-231.

Epstein, E S, 1969. Stochastic dynamic prediction. Tellus, 21, 739-759.

Farrell, B F, 1982. The initial growth of disturbances in a barotropic flow. J Atmos Sci, 39, 1663-1686.

Farrell, B F, 1988. Optimal excitation of baroclinic waves. J Atmos Sci, 46 (9), 1193-1206.

Lacarra, J F and O Talagrand, 1988. Short range evolution of small perturbations in a barotropic model. Tellus, 40A, 81-95.

Leith, C E, 1974. Theoretical skill of Monte Carlo forecasts. Mon Wea Rev, 102, 409-418.

Lorenz, E N, 1965. A study of the predictability of a 28-variable atmospheric model. Tellus, 27 (3), 321-333.

Molteni, F and T N Palmer, 1993. Predictability and finite-time instabilities of the northern winter circulation. Q J R Meteorol Soc, 119, 269-298.

Mureau, R, F Molteni and T N Palmer, 1993. Ensemble prediction using dynamically-conditioned perturbations. Q J R Meteorol Soc, 119, 299-323.

Rabier, F and P Courtier, 1992. Four-dimensional assimilation in the presence of baroclininc instability. Q J R Meteorol Soc, 118, 649-672.

Strang, G, 1986. Introduction to applied mathematics. Wellesley-Cambridge Press, 758 pp.

Table 1 Performances of the EPS at fc day 7 and 10, from the experiments run with the OPE and the c03 SVs. For each experiment, the 1st and the 2nd lines of the table shows the number of perturbed forecasts with AC inside a specified AC interval, the 3rd and the 4th line the number of perturbed forecast better than the control and the T213 forecasts. The last two lines of the table reports the AC of the control and of the T213 at fc day 7 and 10.

		fc day 7	fc day 10
OPE	AC > 70%	9	1
	70% > AC > 60%	15	8
	Pert. better Contr.	18	4
	Pert. better T213	8	13
c03	AC > 70%	11	3
	70% > AC > 60%	9	3
	Pert. better Contr.	17	4
	Pert. better T213	10	15
	Control AC	63%	66%
	T213 AC	71%	52%

Table 2 Experiments characteristics

Experiment	OTI	LPO area
OPE	36 h	global
cO2	36 h	NH
cO3	36 h	NH with lat > 30
cO4	36 h	Europe (-45<lon<45;30<lat<80)
cO5	7 days	" "

Table 3 Similarity indices computed between the first 20 most unstable SVs of the experiments reported in Table 2.

%	OPE	cO2	cO3	cO4	cO5
OPE	--	82	50	11	11
cO2		--	50	12	10
cO3			--	21	17
cO4				--	11
cO5					--

Table 4 List of the OPE and c02 SVs characterized by the largest norm projection onto the unstable sub-space generated by the first 20 most unstable c05 SVs.

Experiment	SV-number	% explained
OPE	15	35
	13	33
	8	15
	2	14
cO2	15	32
	20	31
	18	19
	8	15

Table 5 Projection matrix computed between the first 20 most unstable SVs of the c02 and the OPE experiments (each matrix element is the nearest integer to the squared scalar product, in %). The first row identifies the OPE SV number, and the first column the c02 SV number. The last row shows the % of the norm of each OPE SV explained by the c02 unstable sub-space, and the last element of each column is the % of the norm of each c02 SV explained by the OPE unstable sub-space. A star characterizes the 16 SVs selected by the selection algorithm, when the algorithm is applied to each SV set to construct the EPS IC.

	1*	2*	3*	4*	5*	6*	7*	8*	9*	10*	11*	12*	13*	14	15*	16*	17	18*	19	20	
1*	92	1	0	1	0	0	0	0	2	1	0	0	0	0	0	0	0	0	0	0	98
2*	0	3	74	15	0	0	0	0	1	3	0	0	0	0	0	0	0	0	0	0	97
3*	1	80	2	0	1	11	0	0	0	0	0	0	0	0	0	0	0	0	0	0	96
4*	1	0	12	67	14	1	3	0	0	0	0	0	0	0	0	0	0	0	0	0	98
5*	0	2	1	2	54	5	31	0	0	0	0	0	0	0	0	0	0	1	0	0	97
6*	0	5	1	1	3	25	37	1	8	2	0	5	0	5	0	0	0	0	0	0	96
7*	0	2	1	7	16	39	12	1	0	8	0	0	0	1	0	0	8	1	1	0	97
8*	0	0	0	0	0	1	3	88	2	0	0	0	0	0	0	0	1	0	0	0	96
9*	0	0	2	0	1	0	0	1	7	20	0	48	0	3	1	0	4	5	0	0	92
0*	0	0	1	0	1	0	3	0	3	23	8	4	1	24	1	1	1	9	7	1	88
11*	0	0	0	0	0	1	0	1	5	2	66	0	4	8	0	0	0	3	0	1	93
12*	2	0	0	0	0	5	0	3	40	3	13	1	1	1	0	0	18	1	0	0	88
13	0	0	0	0	1	0	0	0	3	1	0	1	0	25	1	0	0	35	13	1	81
14	0	1	0	0	0	3	3	0	7	7	1	24	0	4	0	0	4	1	2	0	59
15*	0	0	0	0	0	1	0	1	0	2	1	1	70	0	0	1	5	0	1	1	85
16	0	1	0	0	2	4	2	0	5	13	1	0	10	6	1	0	11	2	7	4	70
17*	0	0	0	0	0	0	0	0	0	1	1	0	0	6	31	0	2	4	2	1	49
18*	0	0	0	0	0	0	0	0	1	2	0	1	0	0	49	2	2	5	1	0	65
19	0	0	0	1	2	0	1	0	4	0	0	0	0	0	3	0	20	1	0	2	35
20*	0	0	0	0	0	0	0	0	1	1	1	0	0	1	0	0	2	8	48	3	66
	98	96	96	97	97	95	96	96	89	89	93	88	87	85	86	5	79	76	82	14	

Table 6 Springtime similarity indices computed between the unstable sub-spaces generated by the first 20 most unstable SVs, computed without the LPO and with the LPO applied to constraint the SV growth to the grid points with $\lambda \geq 30$.

	02/05/92	09/05/92	16/05/92
$s(global;\lambda \geq 30;20$	39%	22%	17%

14.02.93 12Z - ANALYSIS

a)

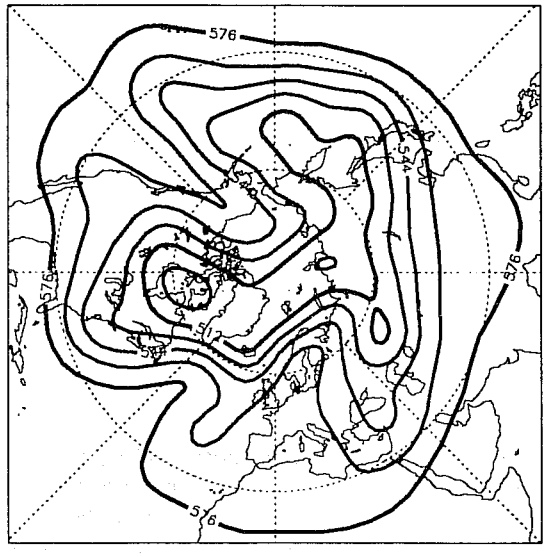

21.02.93 12Z - ANALYSIS

b)

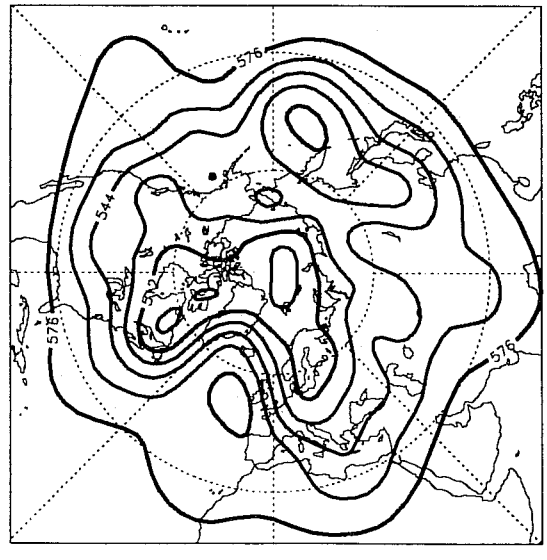

Fig 1 500 hPa geopotential height field at 12GMT of the 14.02.93 (panel a), and of the 21.02.93 (panel b). Contour intervals are drawn every 160 m.

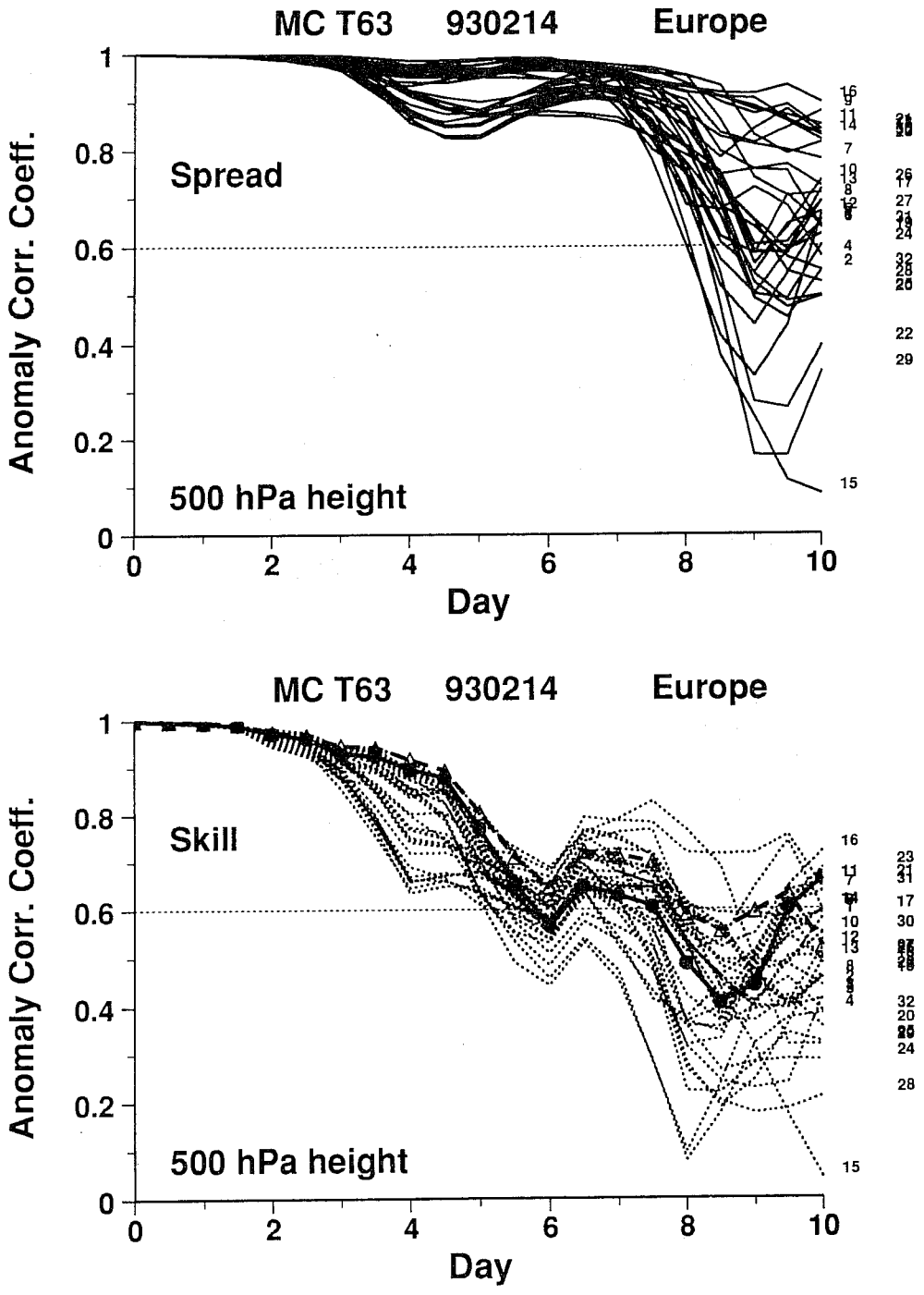

Fig 2 Spread and skill scores of the 14.02.93 EPS 500 hPa geopotential height field. Top panel: spread between each member and the control, measured as AC. Bottom panel: skill of the T63 control (solid line with full dots), of the T213 forecast (dashed line with triangle), and of the 32 perturbed members (dotted lines). The numbers on the right-hand side refer to the member number.

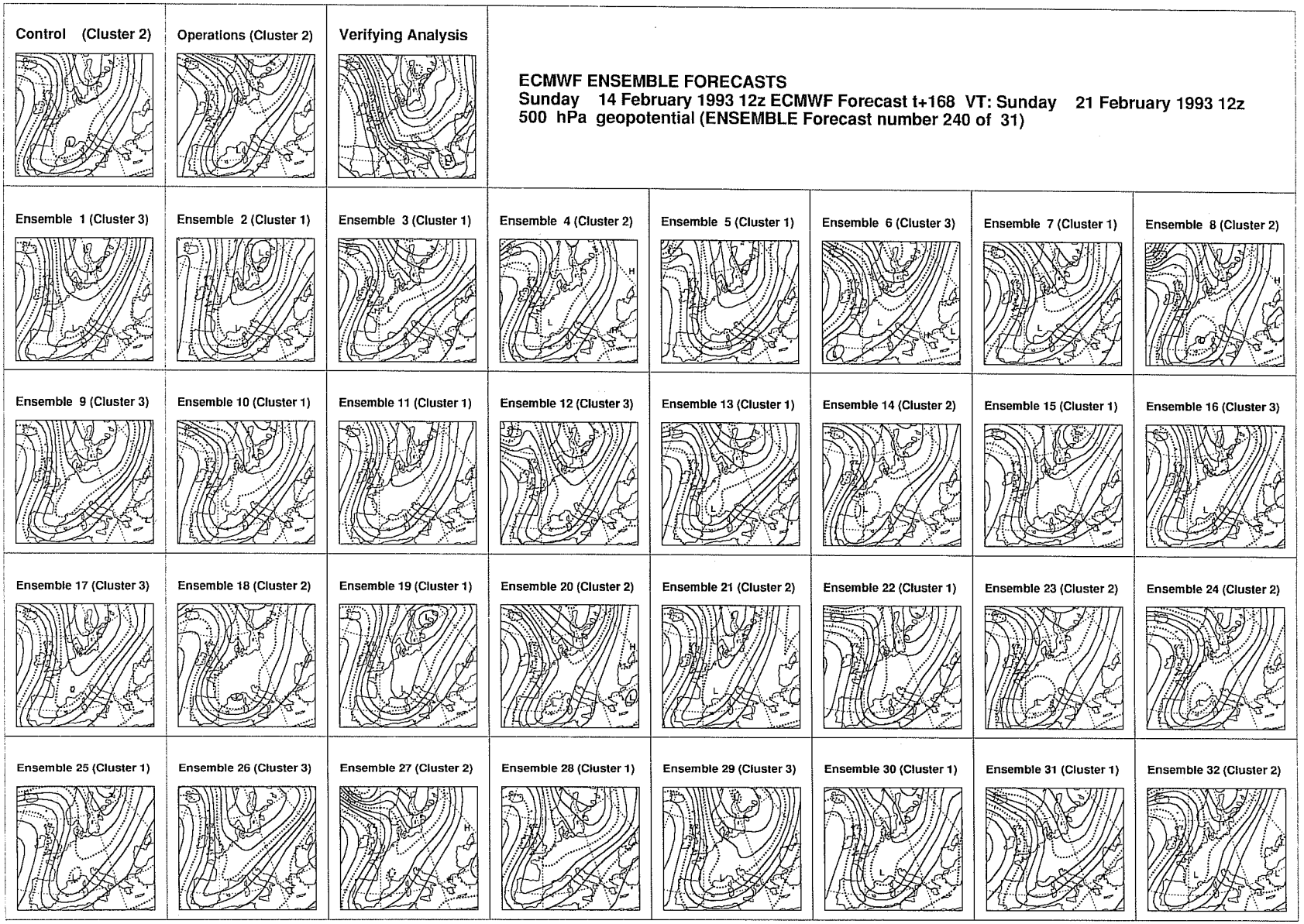

Fig 3 500 hPa geopotential height at fc day 7 of the EPS forecasts and of the verifying analysis over the European area.
Top-left 1st panel: control forecast. Top-left 2nd panel: high resolution operational forecast.
Top 3rd panel: verifying analysis. From the 2nd to the 5th row: 32 EPS perturbed forecasts. Contour isolines are drawn every 60 m.

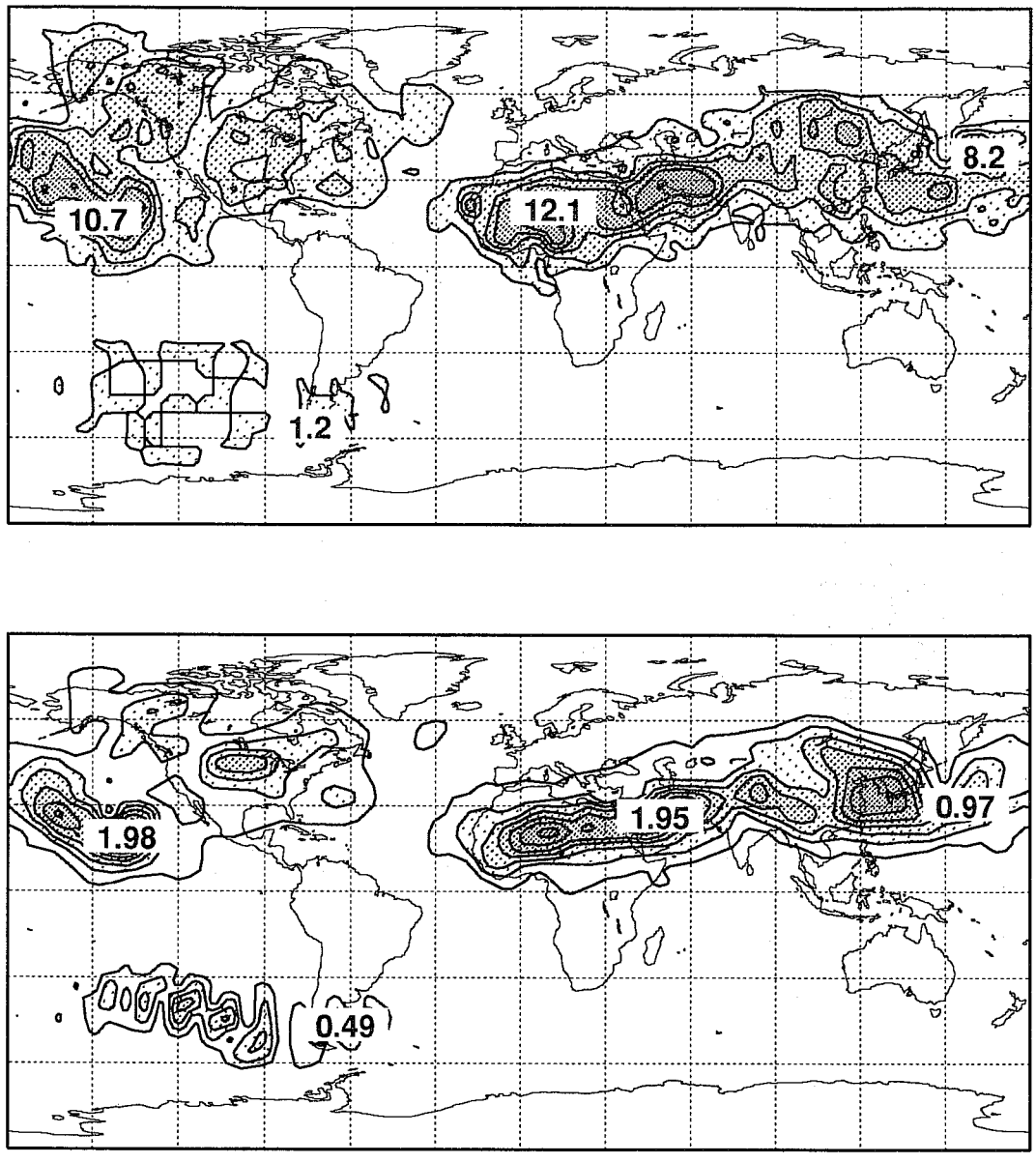

Fig 4 Overlap factor (top panel) and RMS amplitude (bottom panel) of the OPE selected perturbations, at model level 11 (i.e. almost 500 hPa). The RMS amplitude refers to the temperature component of the state vector. Contour isolines are drawn every 2 starting from 1 in the top panel, and every 0.25 degrees starting from 0.125 degrees in the bottom panel.

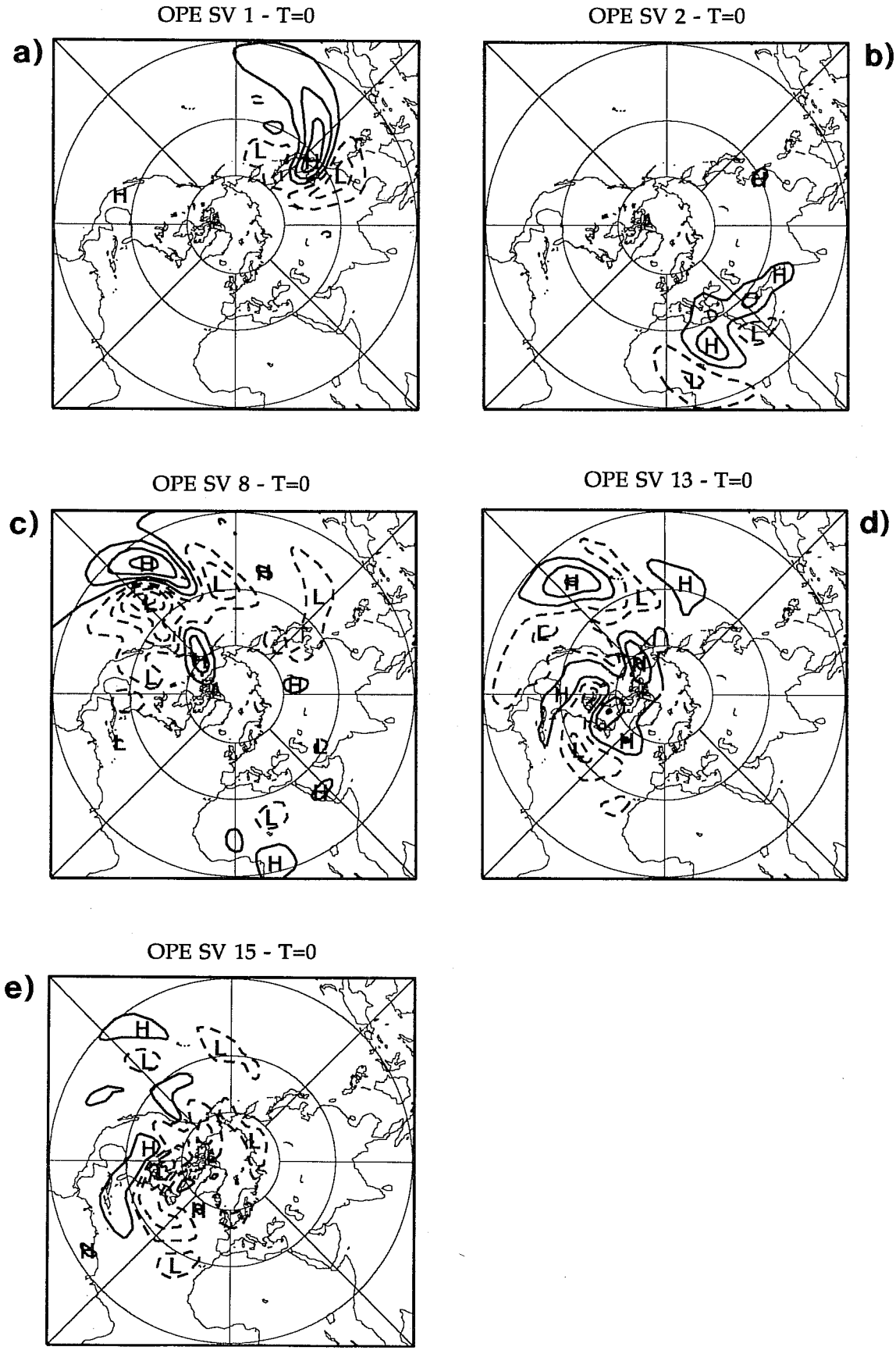

Fig 5 Streamfunction at model level 11 of 5 OPE SVs. The 1st (panel a), 2nd (b), 8th (c), 13th (d) and 15th (e) SVs are plotted. The SVs are normalized to have unitary total energy norm. Contour isolines are drawn every 0.5 10^{-8}, with solid/dashed isolines referring to positive/negative values.

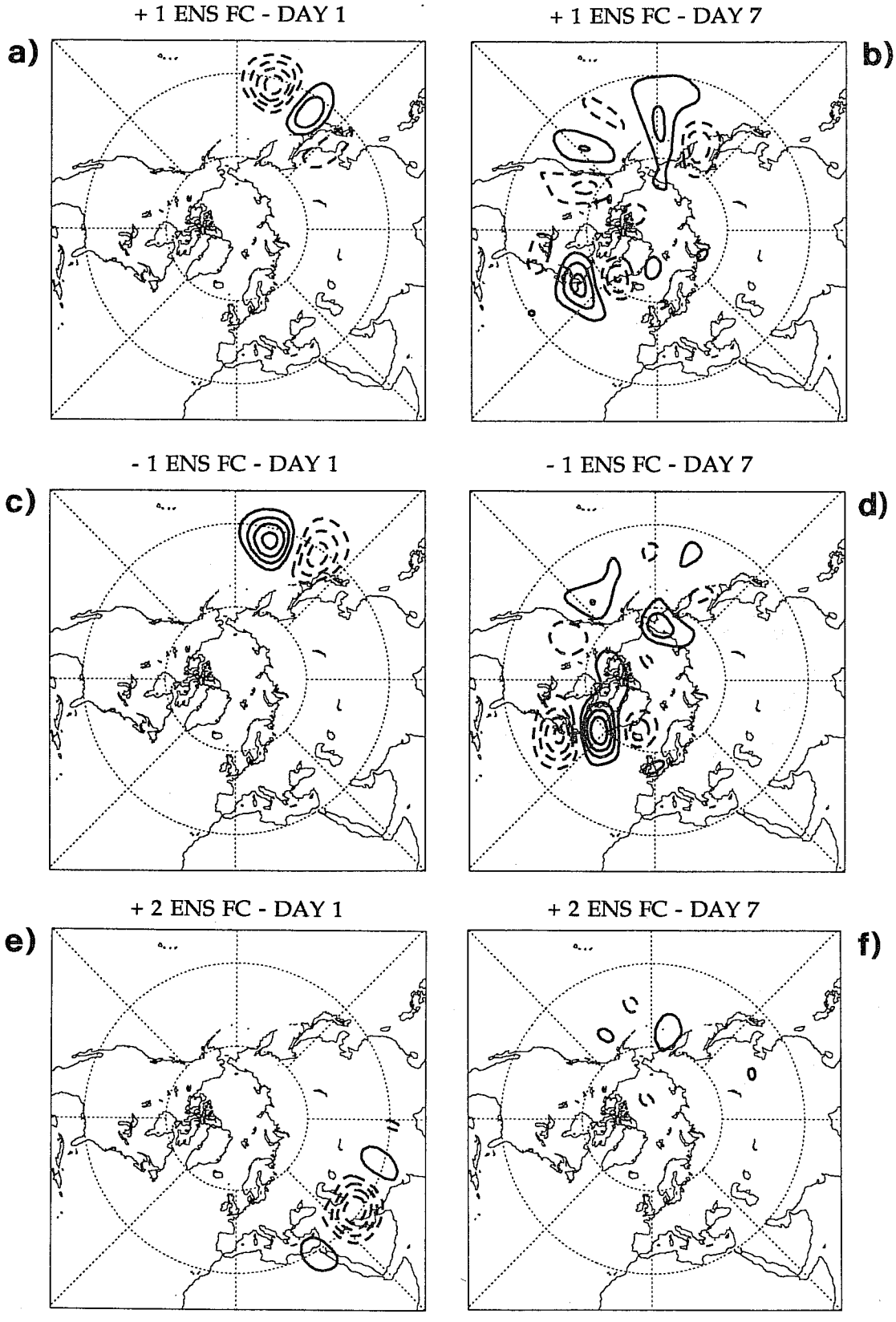

Fig 6 Spread between the perturbed forecasts and the control, of the perturbed forecasts with IC generated adding and subtracting some unrotated SVs, at fc day 1 (left panels) and fc day 7 (right panels), computed using the 500 hPa geopotential height fields. Contour intervals are drawn every 1 m for left panels, and every 5 m for right panels. Panels refers to forecasts as listed below:

Panels a-b: perturbed forecasts generated adding the 1st SV.
Panels c-d: perturbed forecasts generated subtracting the 1st SV.
Panels e-f: perturbed forecasts generated adding the 2nd SV.
Panels g-h: perturbed forecasts generated subtracting the 2nd SV.
Panels i-l: perturbed forecasts generated adding the 8th SV.
Panels m-n: perturbed forecasts generated subtracting the 8th SV.

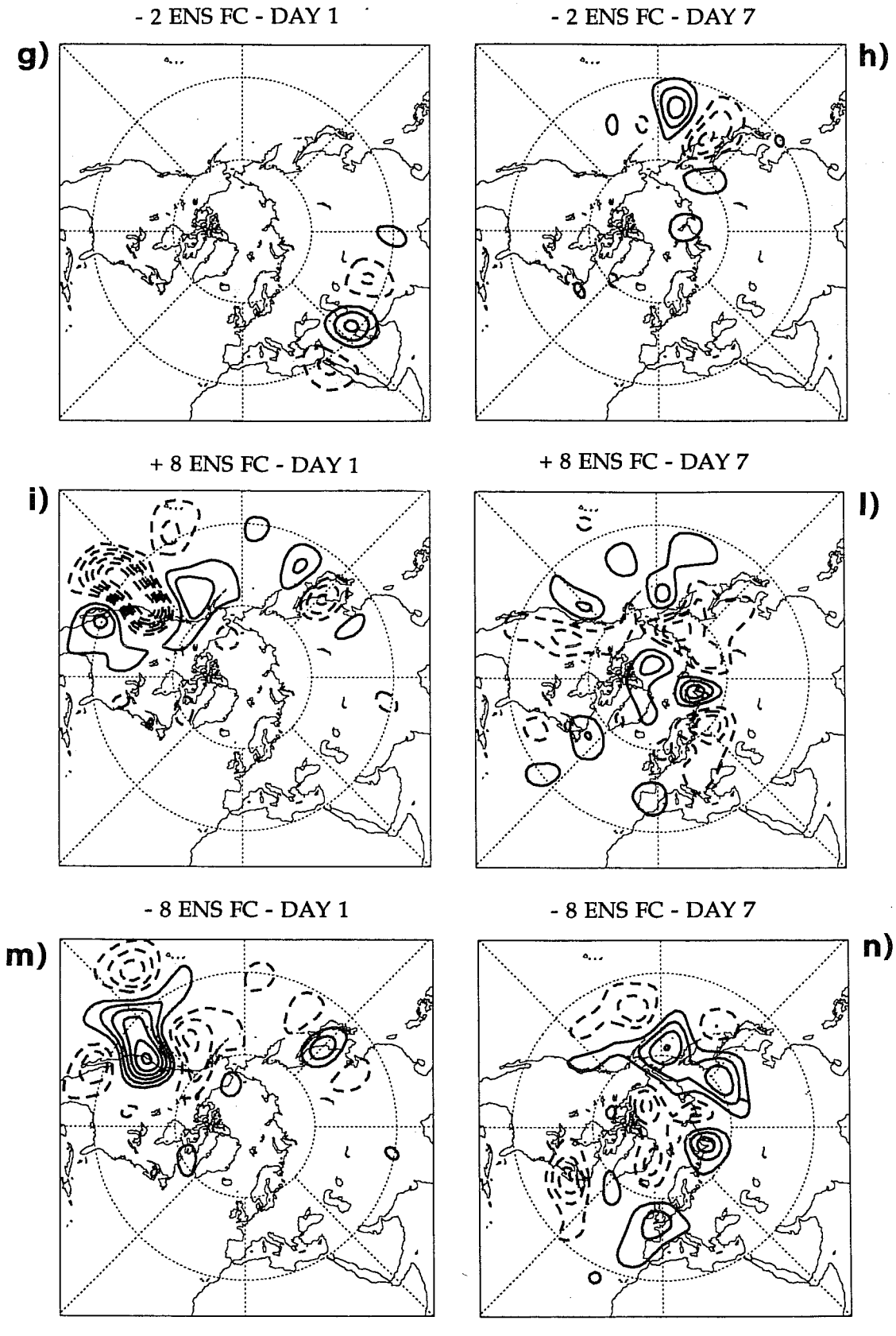
- 2 ENS FC - DAY 1
- 2 ENS FC - DAY 7
g)
h)
+ 8 ENS FC - DAY 1
+ 8 ENS FC - DAY 7
i)
l)
- 8 ENS FC - DAY 1
- 8 ENS FC - DAY 7
m)
n)

Fig 6 Contd

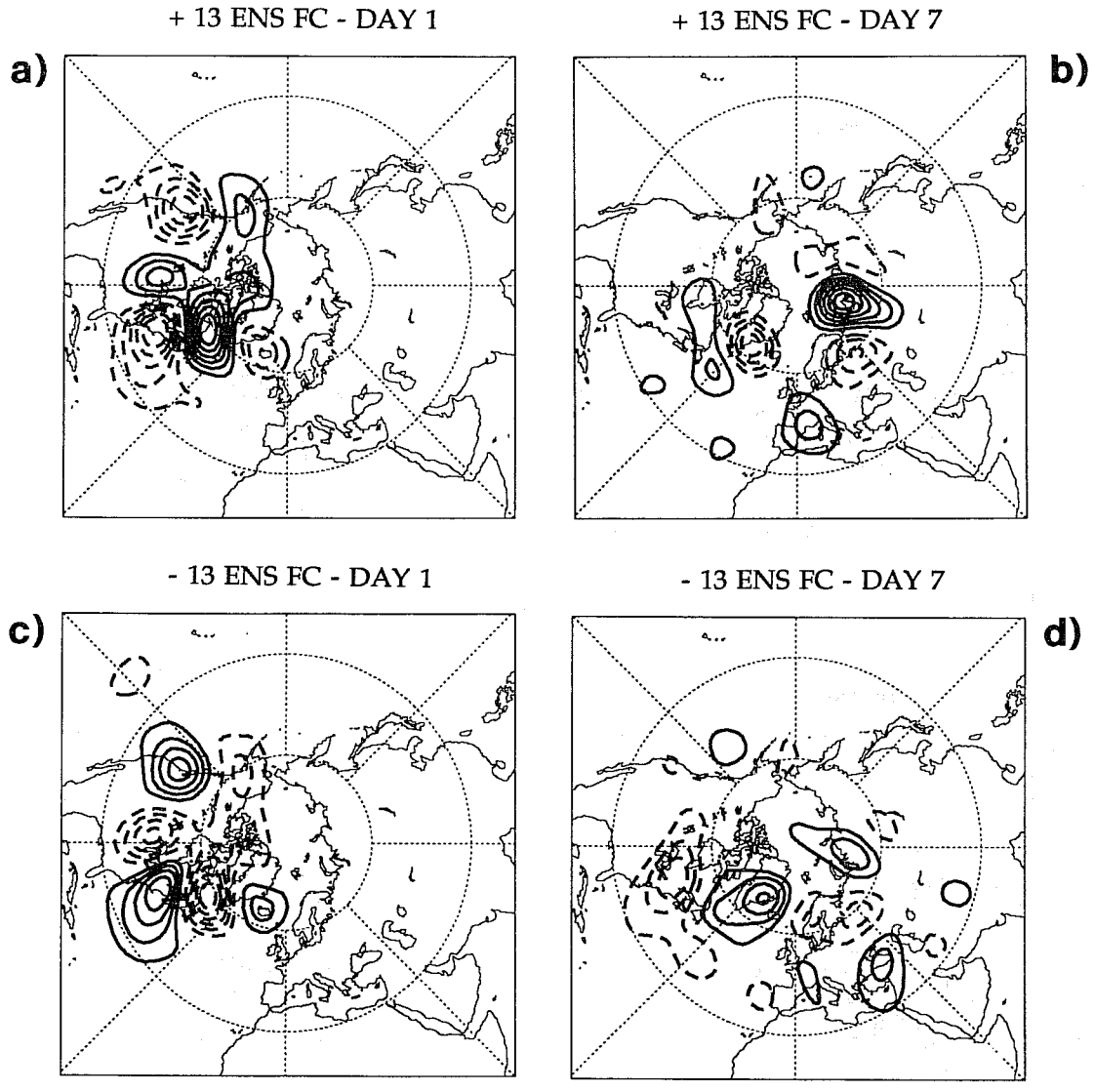

Fig 7 As Fig 6. Panels refers to forecasts as listed below:
Panels a-b: perturbed forecasts generated adding the 13th SV.
Panels c-d: perturbed forecasts generated subtracting the 13th SV.

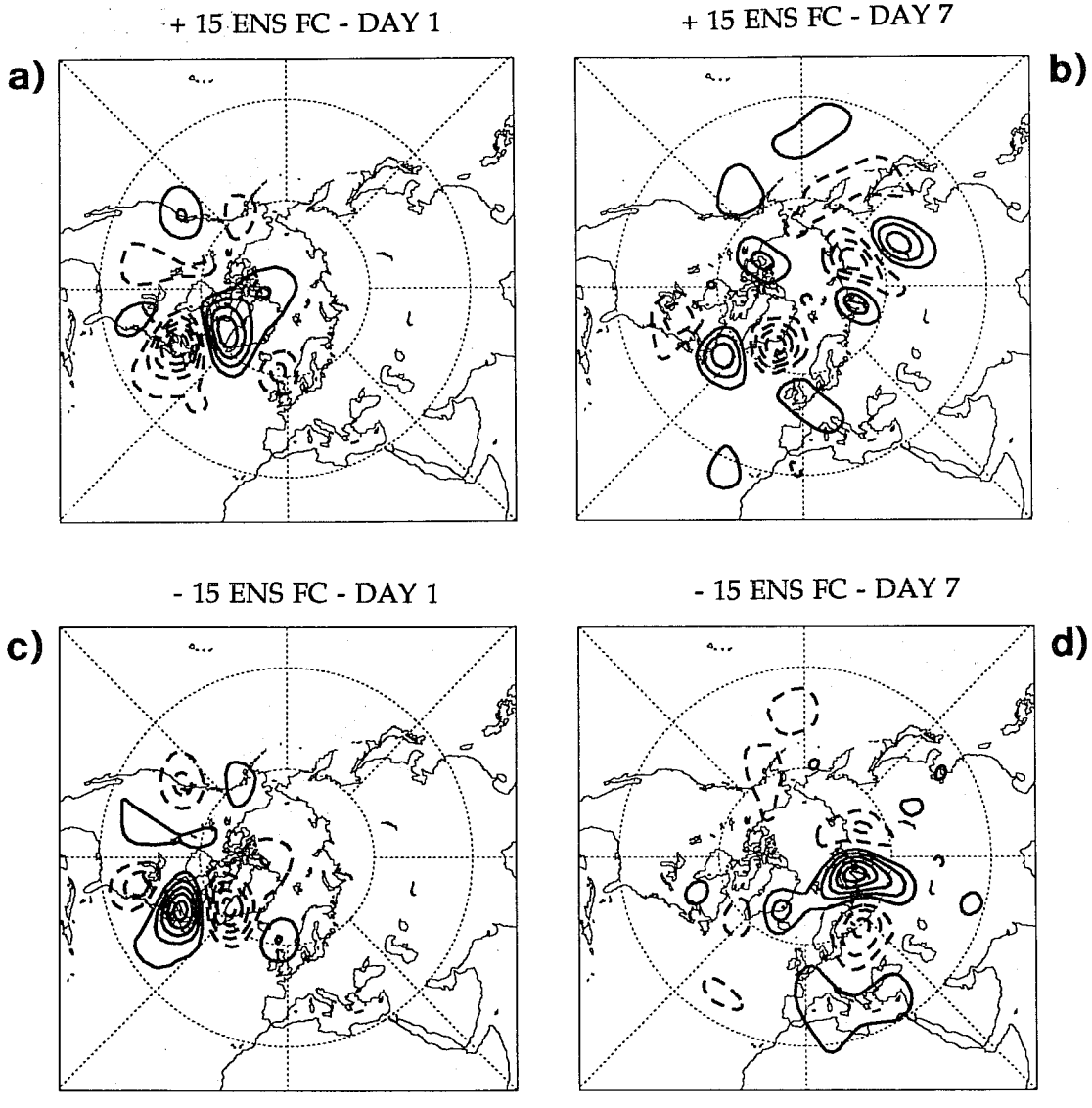

Fig 8 As Fig 6. Panels refers to forecasts as listed below:
Panels a-b: perturbed forecasts generated adding the 15th SV.
Panels c-d: perturbed forecasts generated subtracting the 15th SV.

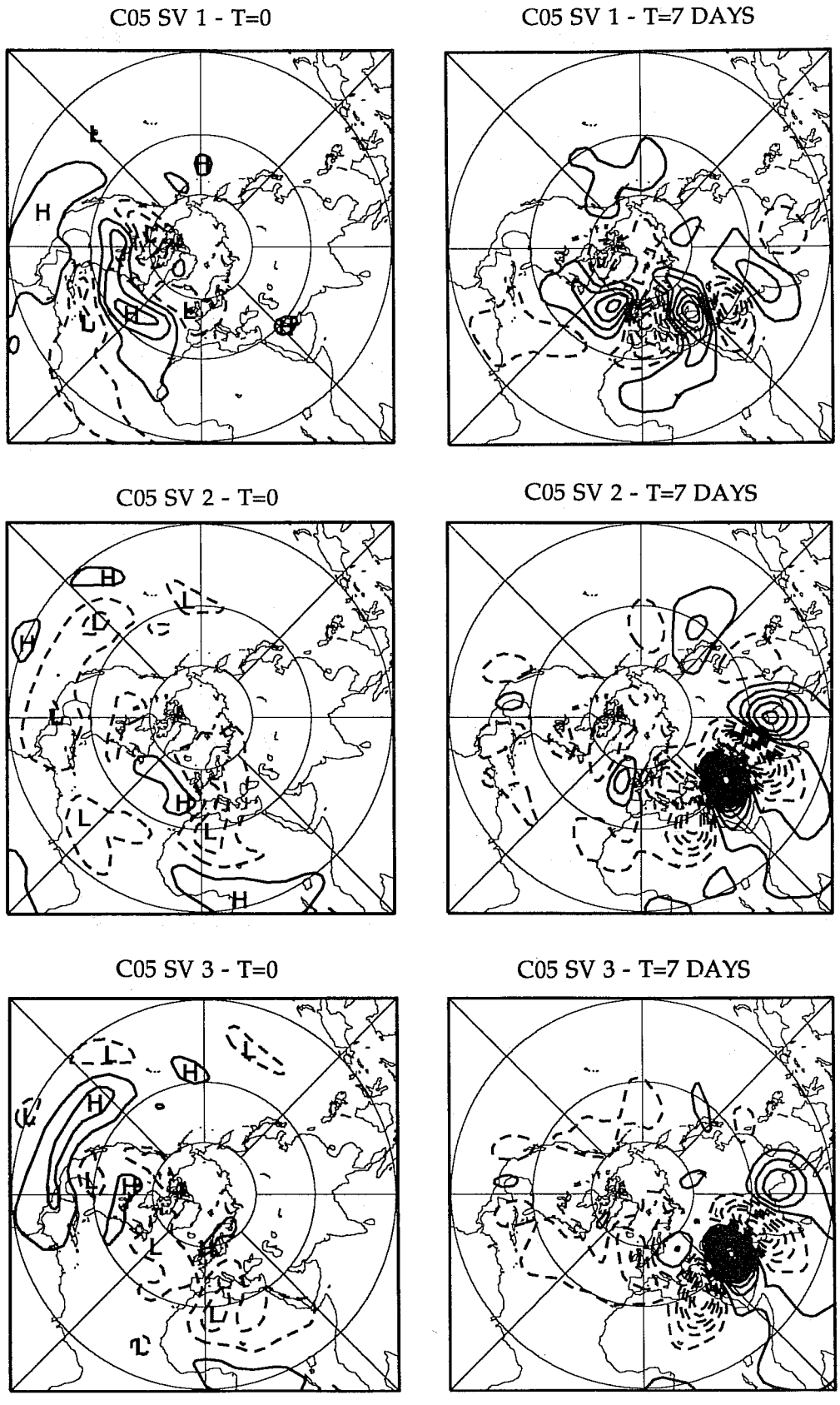

Fig 9 Streamfunction of the first 6 c05 SVs, at initial (left panels) and final time (right panels). The SVs are sorted in decreasing order from top to bottom. They are normalized to have at initial time unitary total energy norm. At initial time, contour isolines are drawn as in Fig 5, while the contour interval is 20 times larger at final time.

C05 SV 4 - T=0

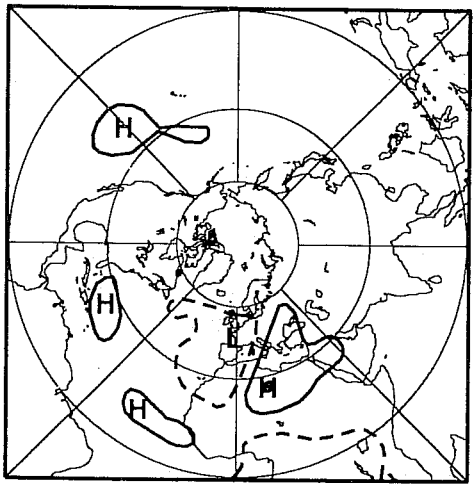

C05 SV 4 - T=7 DAYS

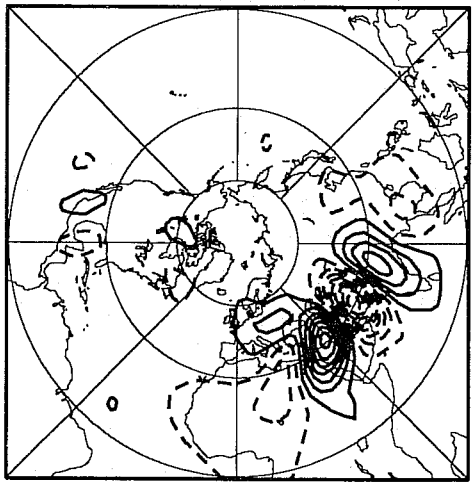

C05 SV 5 - T=0

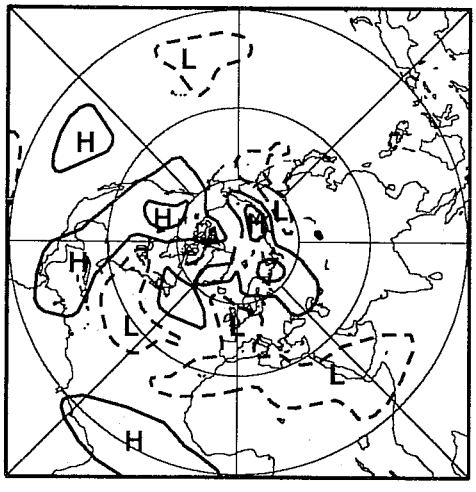

C05 SV 5 - T=7 DAYS

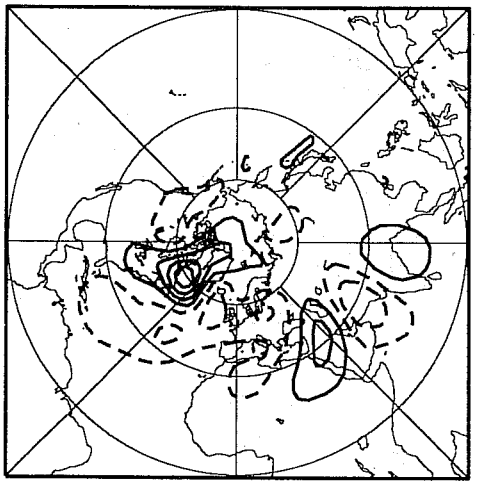

C05 SV 6 - T=0

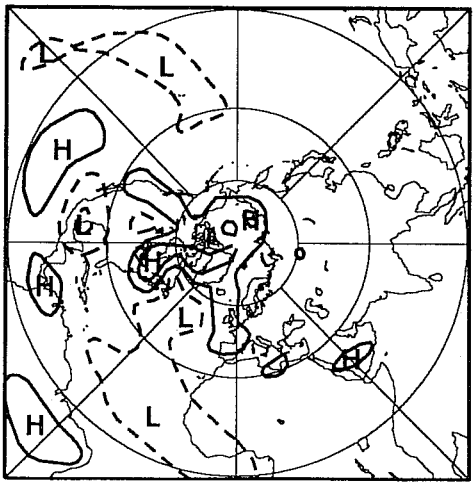

C05 SV 6 - T=7 DAYS

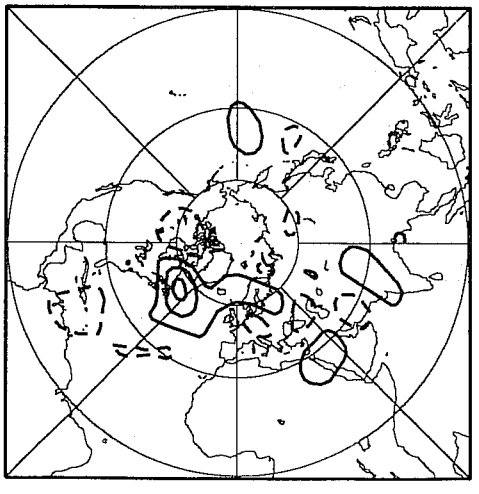

Fig 9 Contd

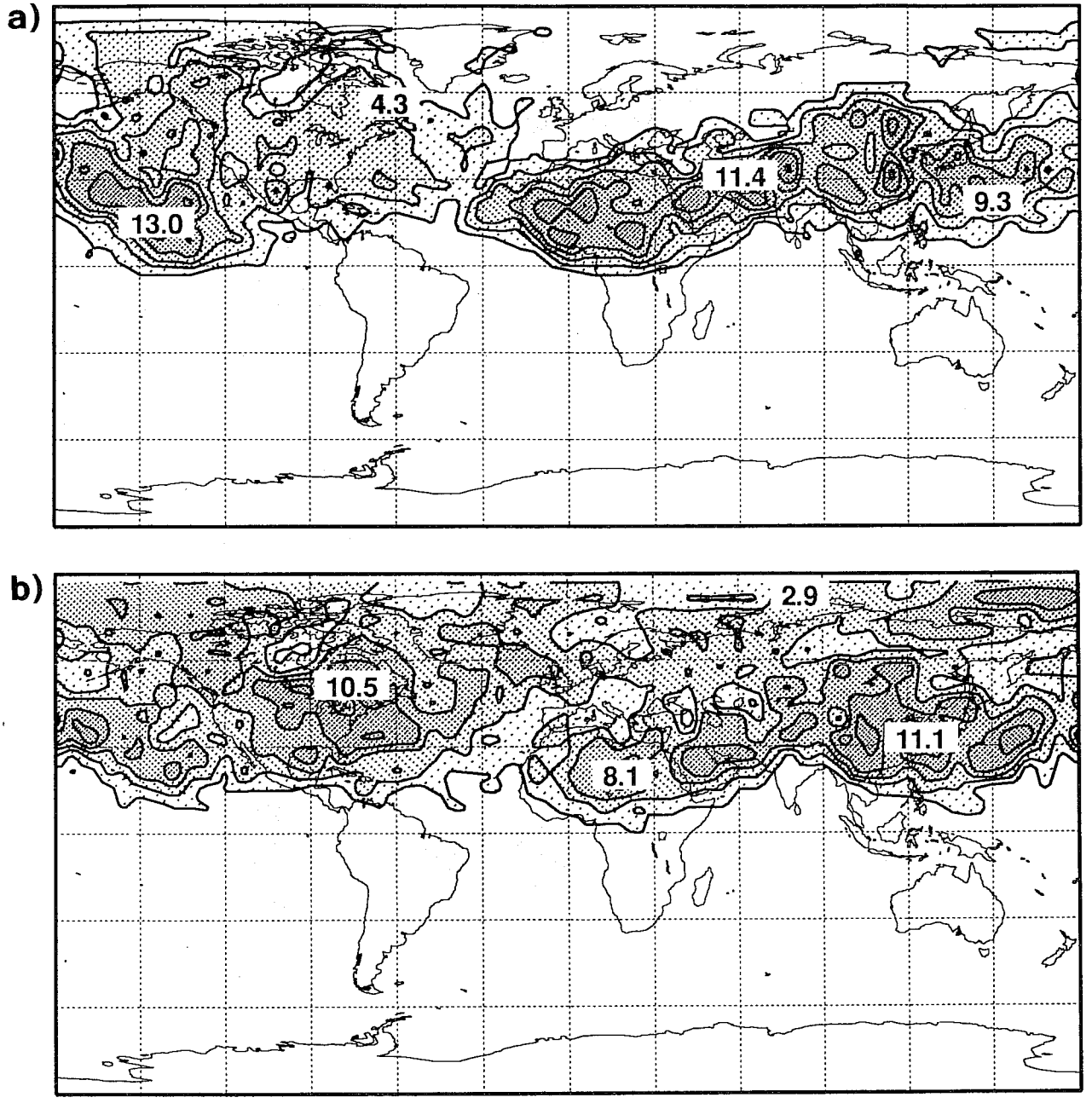

Fig 10 Overlap factors of the selected c02 (panel a) and the c03 (panel b) SVs. Contour isolines are drawn as in Fig 4a.

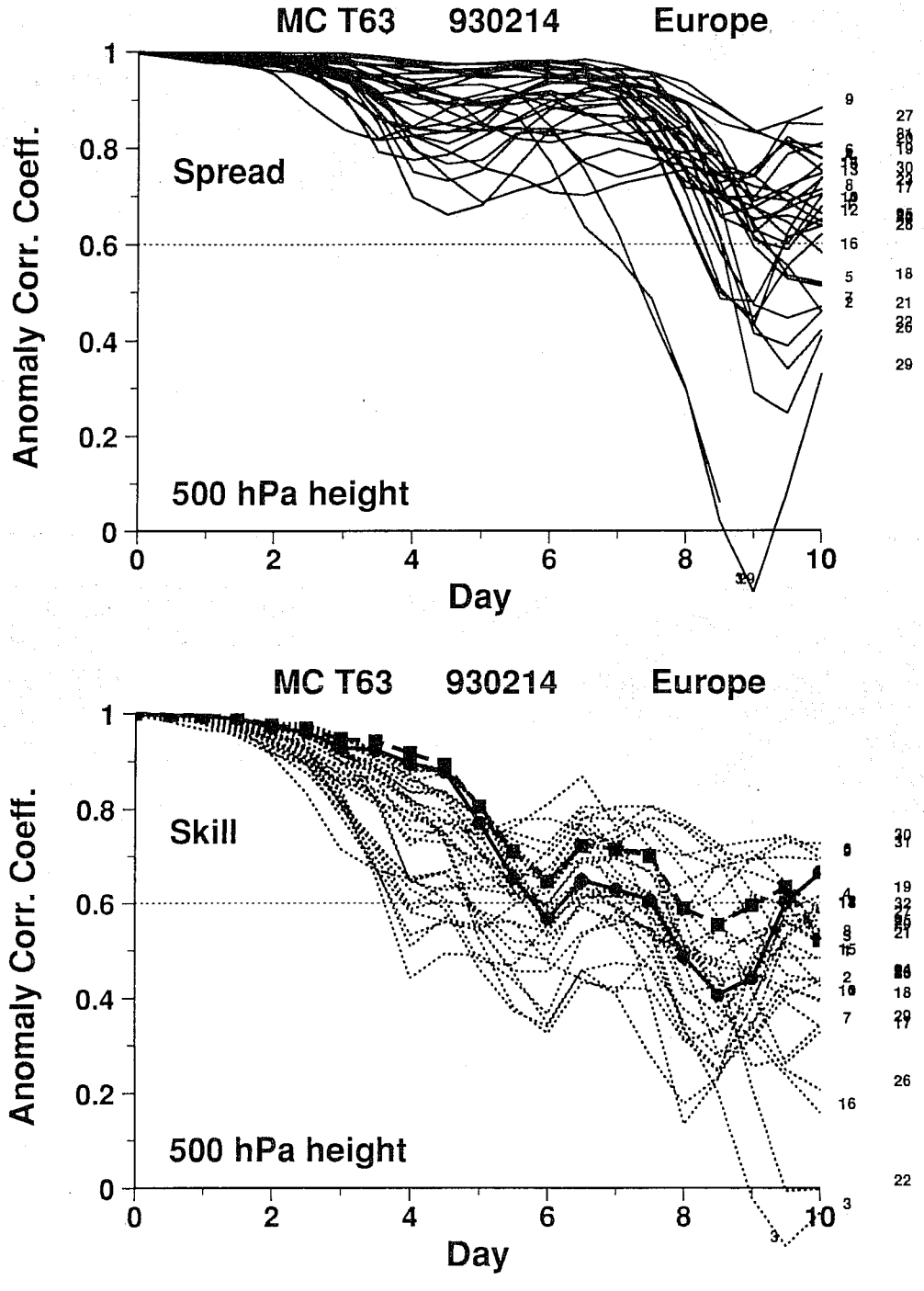

Fig 11 Spread and skill scores of the EPS run with the IC generated from the localized c03 SVs, as in Fig 2.

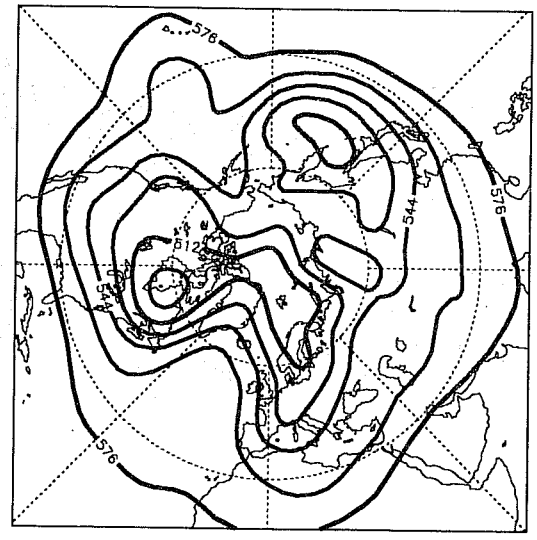

Fig 12 500 hPa geopotential height field, at fc day 7, of the 30th member of the EPS run with the IC generated from the localized c03 SVs. Contour isolines are drawn as in Fig 1.

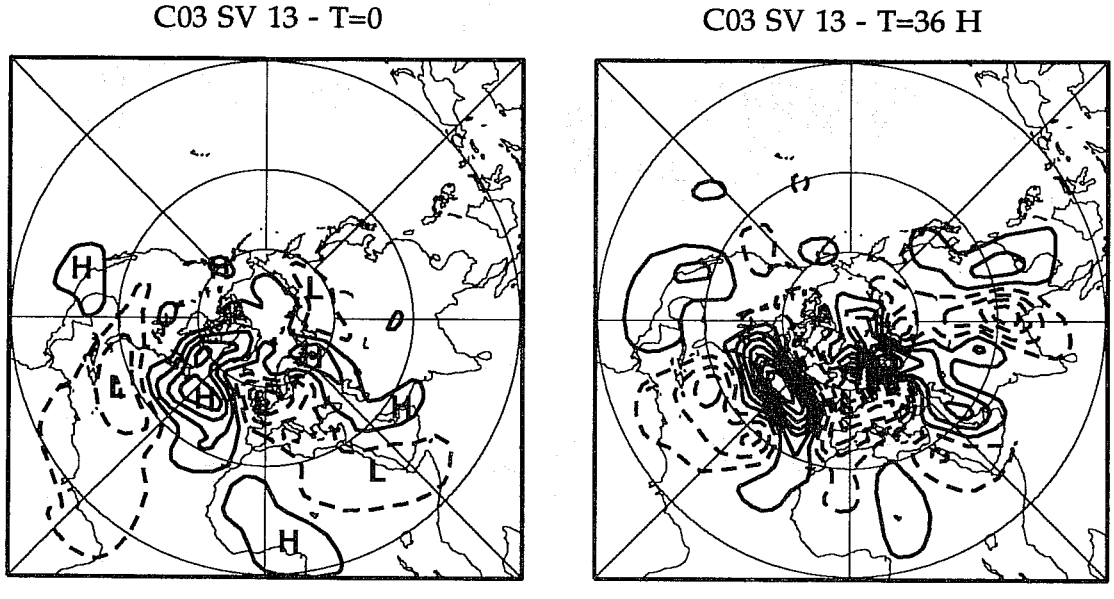

Fig 13 Streamfunction, at model level 11, of the 13th c03 SV, at initial (left panel) and after 36h of linear time integration (right panel). At initial time, contour isolines are drawn as in Fig 5, while with a 2 times larger interval at final time.

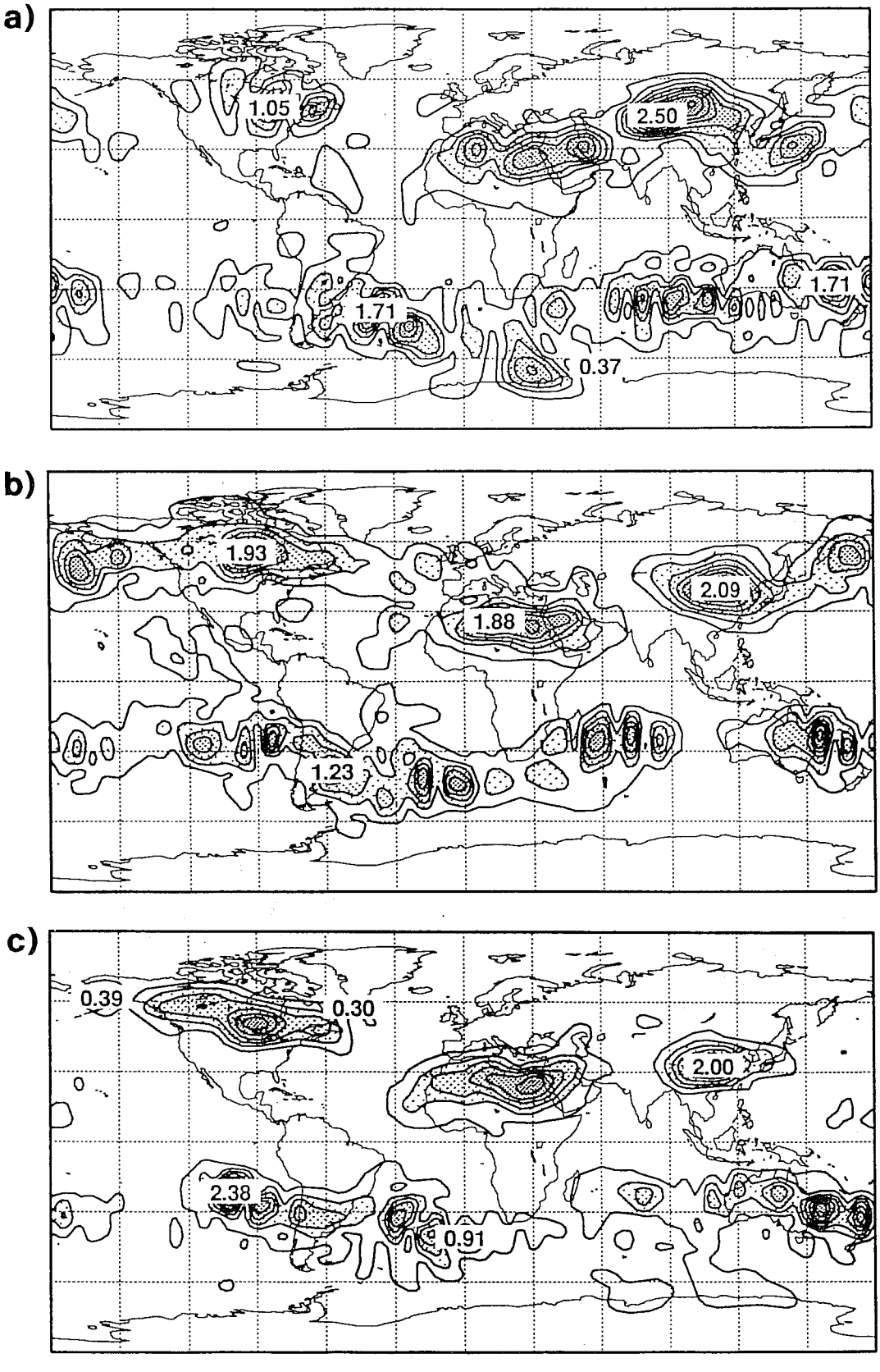

Fig 14 RMS amplitude of the selected perturbations (temperature at model level 11) for the SVs computed without the LPO, for the following starting dates: 02.05.93 (panel a), 09.05.93 (panel b) and 16.05.93 (panel c). Contour isolines are drawn as in Fig 4b.

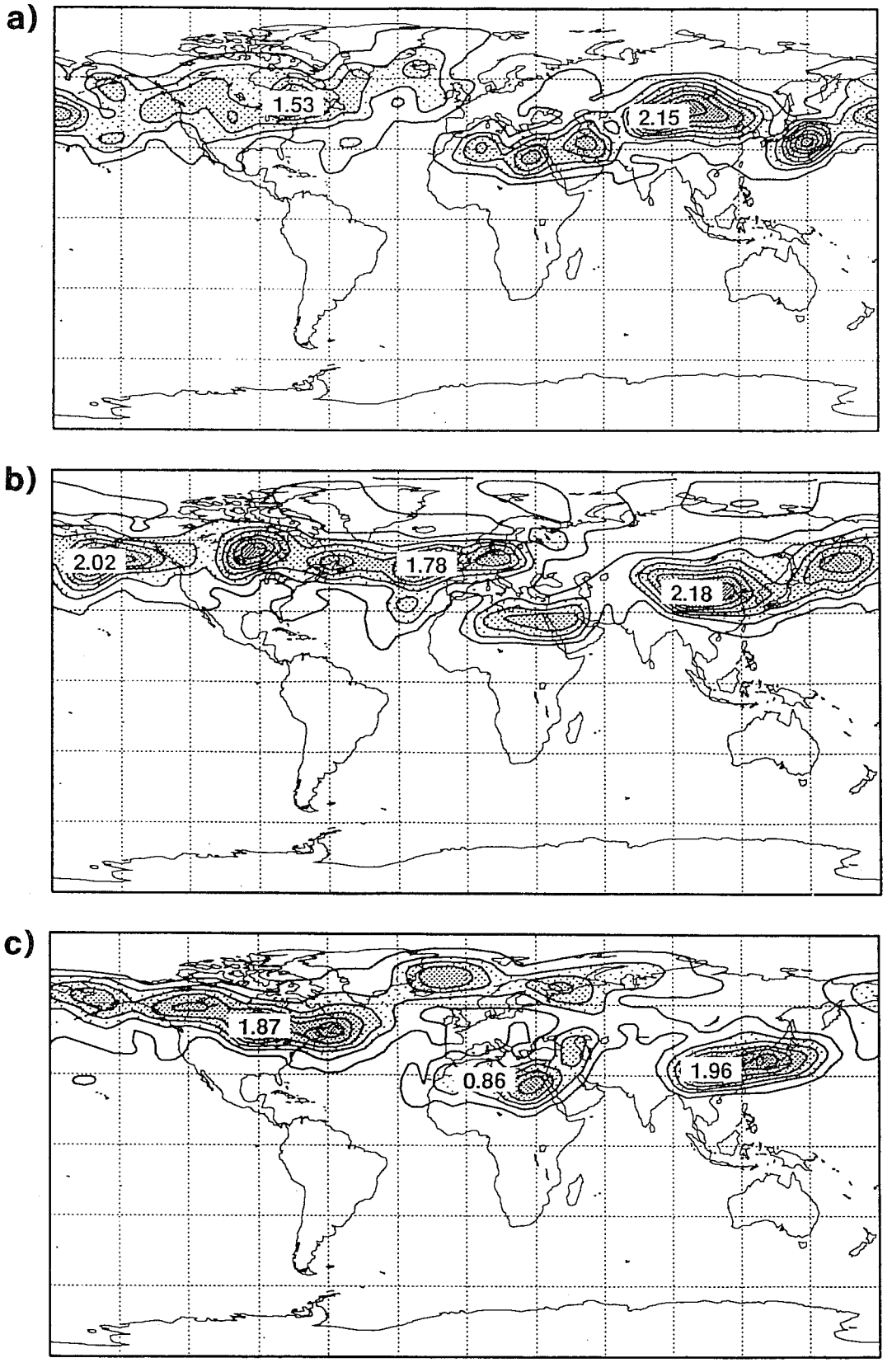

Fig 15 As Fig 14, but for the SVs constraint to be confined by the LPO to the grid points with $\lambda \geq 30$. Contour isolines are drawn as in Fig 4b.